THE ASTROPHYSICAL JOURNAL, 444:21–40, 1995 May 1

STRUCTURE AND PHOTOMETRY OF AN $I < 20.5$ GALAXY SAMPLE FROM THE *HUBBLE SPACE TELESCOPE* MEDIUM DEEP SURVEY[1]

ANDREW C. PHILLIPS, MATTHEW A. BERSHADY,[2,3] AND DUNCAN A. FORBES
University of California Observatories/Lick Observatory, University of California, Santa Cruz, CA 95064

DAVID C. KOO, GARTH D. ILLINGWORTH, AND DAVID B. REITZEL
University of California Observatories/Lick Observatory and Board of Studies in Astronomy and Astrophysics, University of California, Santa Cruz, CA 95064

RICHARD E. GRIFFITHS
Bloomberg Center for Physics and Astronomy, Johns Hopkins University, 3400 North Charles Street, Baltimore, MD 21218

AND

ROGIER A. WINDHORST
Department of Physics and Astronomy, Arizona State University, Tempe, AZ 85287-1504
Received 1994 March 14; accepted 1994 October 20

ABSTRACT

A set of 100 faint galaxies from nine *Hubble Space Telescope* Wide Field Camera I-band images have been analyzed as part of the Medium Deep Survey (MDS) Key Project. This sample reaches a depth of $I \lesssim 20.5$ (corresponding to $B \sim 22$–23) and complements the first set of fainter galaxies analyzed by the MDS team. Images were deconvolved using the Lucy-Richardson algorithm and a newly developed procedure designed to yield a more reliable determination of structure in the low-S/N regime. These deconvolved images were used to characterize the structure of the galaxies through quantitative measurements of total magnitudes, half-light radii, exponential disk scale lengths, and disk-to-total ratios. Extensive testing was done to establish the validity of the procedures used and to characterize the degree of systematic errors present in the analysis techniques.

The observed size-magnitude distributon appears consistent with a scenario in which luminous galaxies have evolved little in intrinsic luminosity, size, or structure over recent epochs in a "normal" cosmology ($0 < q_0 < 0.5$ and $\Lambda_0 = 0$). The predicted nonevolving distributions were based on models designed to fit existing counts, colors, and redshifts of faint galaxies and on the observed correlations between metric rest-frame size and luminosity found in a nearby galaxy sample studied by Kent (1984, 1985). The typical galaxy in our sample is expected to be at $z \simeq 0.3$, and to have a luminosity ~ 0.5 mag fainter than L^* and a half-light radius of $\sim 1''$ or ~ 6 kpc ($H_0 = 50$ km s^{-1} Mpc^{-1}).

The observed distribution of disk-to-total ratios, while uncertain, is in agreement with that of Kent's sample and thus supports the view that substantial evolution has not occurred over the look-back times characteristic of our sample.

Subject headings: cosmology: observations — galaxies: fundamental parameters — galaxies: photometry — surveys

1. INTRODUCTION

The nature of evolution among faint field galaxies remains an active area of research and debate. The bulk of the research has focused on counts, clustering properties, integrated colors, and spectral characteristics as a function of redshift (for an overview, see Koo & Kron 1992; Lilly 1993). In contrast, very limited work has been undertaken to explore the morphology and structure of such galaxies (e.g., Giraud 1992; Lilly 1993), largely because, even under excellent seeing conditions from the ground, typical galaxies fainter than $B \sim 20$ remain only marginally resolved. However, information on morphology and structure provide independent probes of galaxy evolution and clues to the physical processes that govern this evolution. A few examples of this would include finding a change in the relative frequency of Hubble types among field galaxies, perhaps due to spirals transforming themselves into earlier type galaxies through merging; discovering a higher incidence of merger or interaction signatures, such as strong asymmetries or tidal tails, that may accompany unusually blue colors; or quantifying a change with look-back time in the tight "fundamental plane" relationships found locally among luminosities, length scales, surface brightnesses, and internal velocities of galaxies (Kormendy & Djorgovski 1989, and references therein).

As noted above, the strategy of using morphology and structural information in faint galaxy evolution research is still in its infancy compared to the more mature techniques of tracking photometric or clustering evolution. The best ground-based images taken under unusually good seeing conditions (e.g., Lavery, Pierce, & McClure 1992; Giraud 1992; Lilly 1993) are a good start but have not provided the required quantitative results. Results in this area can now be dramatically improved with the *Hubble Space Telescope* (*HST*).

HST is particularly well suited to the detection of structure in faint galaxies because of the high spatial resolution. Even

[1] Based on observations with the NASA/ESA *Hubble Space Telescope*, obtained at the Space Telescope Science Institute, which is operated by AURA, Inc., under NASA contract NAS 5-26555.

[2] Hubble Fellow.

[3] Current address: Department of Astronomy and Astrophysics, Pennsylvania State University, 525 Davey Laboratory, University Park, PA 16802.

with the aberrated images prior to the *HST* refurbishment mission, the contrast of features within galaxies (spiral arms, bars, etc.) is greatly enhanced over what can be discerned from ground-based images. A less obvious reason is that the sky background from space is substantially lower than that from the ground. Near the ecliptic pole, the sky seen by *HST* reaches $\sim$22.2 mag arcsec^{-2} in I and $\sim$23.2 mag arcsec^{-2} in V (Windhorst, Mathis, & Keel 1992). This should be compared to the sky brightness at the best terrestrial sites, e.g., $V \sim 22.0$ and $I \sim 19.9$ mag arcsec^{-2} (Geisler 1988).

Among the *HST* programs designed to explore faint galaxy structure is the Medium Deep Survey (MDS), one of three Key Projects of the *HST*. Several MDS efforts are already well underway to explore the morphology of faint galaxies, each effort taking different approaches to extract the morphology and photometry from the *HST* images. For example, multi-orbit data for 3C 273 have been analyzed by Griffiths et al. (1994a, hereafter G94); deconvolved images and redshifts of brighter galaxies have been presented by Windhorst et al. (1994) and further studies are in progress by Mutz et al. (1994); and maximum-likelihood galaxy model fits to unrestored images are in progress by Ratnatunga et al. (1995). In addition, a large database of faint galaxy parameters as determined by the Faint Object Classification and Analysis System (FOCAS) and maximum-likelihood methods is being prepared (Neuschaefer et al. 1995).

In this paper we examine galaxies brighter than about $I \sim 20.5$ observed during the first 9 months of operation of the MDS using the first Wide Field Camera (WFC-I). We chose this magnitude cutoff because tests with simulated galaxy models show that we can expect to reliably measure structural parameters for galaxies brighter than $I \simeq 21$ in a single-orbit integration. Our primary goal is to form a database of photometry and structural information suitable for the statistical analysis of the evolution of faint field galaxies. We present here the measurements for 100 galaxies. Future papers will extend the sample to MDS fields observed with WFPC-II (e.g., Forbes et al. 1994; Griffiths et al. 1994b) and will examine individual deep fields to fainter levels and in more detail.

This paper is organized as follows. In § 2, we describe the observations and reduction of the WFC images, sample selection, and deconvolution of galaxy images, followed by descriptions of the techniques used to measure photometric and structural parameters in §§ 3 and 4. These technical sections also include extensive tests of simulated galaxies to determine the reliability of these procedures for our deconvolved images. Readers interested only in the scientific results should proceed to later sections. Additional technical details on the deconvolution procedure developed for low-S/N images are included in an Appendix. We present our galaxy measurements in § 5, and discuss their significance by comparing several measurements (size, magnitude, and disk-to-total luminosity) to a local sample of galaxies in § 6.

2. DESCRIPTION OF THE DATA AND REDUCTION PROCEDURES

A more extensive discussion of the MDS project is given by G94, but we briefly summarize some relevant aspects here. The MDS uses "parallel mode" observations in which an unused instrument, primarily the Wide Field/Planetary Camera (WFPC), takes images of nontargeted fields at the same time that the primary instrument is acquiring data on the targeted object or field. The WFPC field is $\sim$3.5 from the Faint Object Spectrograph (FOS) apertures and $\sim$6′ from the High-Resolution Spectrograph (HRS) and Faint Object Camera (FOC) fields. MDS observations have typically been one or two single-orbit integrations of $\sim$30 minutes each, using the WFC model. However, a few, considerably longer, multiorbit sets of integrations have been obtained. MDS WFC images have generally been obtained in the F785LP ("I_{785}") passband, and when possible in F555W ("V") as well.

2.1. *Data and Sample Selection*

The MDS obtained WFC images of a total of 16 fields between 1992 January and the end of 1992 September. We adopt a naming convention of "MDSW" ("W" for WFC) followed by a chronological sequence number, e.g., W2 for the second WFC field. Of the first 16 fields, seven were excluded from our sample because F785LP images were not available (W7, W8, and W13), the fields were dominated by stars in the Large Magellanic Cloud (LMC) (W6 and W14) or 47 Tuc (W4), or the field was within the outer regions of the nearby, late-type galaxy NGC 4395 (W9). The remaining nine fields, observed in F785LP, are the focus of this paper; the observations are summarized in Table 1. The first and second fields (W1 and W2) are two of the deepest observed for the MDS, with several hours of exposure each. W1 is located 6′ away from 3C 273, and W2 is near the deep galaxy survey region SSA 13 (Lilly, Cowie, & Gardner 1991). A detailed analysis of the W1 field has been carried out by G94 and for six galaxies in W2 by Windhorst et al. (1994).

The WFC has a scale of 0.″1 pixel^{-1}, which means that the sharp core and "tendrils" of the aberrated point-spread function (PSF) (Burrows et al. 1991) are somewhat undersampled. The field of view is 2.′6, but the $\sim$3″ radius of the PSF means that $\sim$0.′2 is effectively lost near the edges of the CCDs where the data are unusable for most deconvolution algorithms. In a few fields, the primary observations were "dithered" or spatially offset between exposures with the net result that the field covered by the final montage of WFC images is larger; unfortuntely, the object images in the overlapping frames have different PSFs and so cannot be simply co-added and processed. In the fields considered here, only W2 and W12 are dithered, and only in W2 have we analyzed images for more than one pointing.

The raw image data were initially reduced using the STScI pipeline, following the method outlined by Lauer (1989). However, there are problems associated with the current pipeline processing, as described in Phillips et al. (1994) and Ratnatunga et al. (1994). In particular, the F785LP pipeline flat-field frames have been shown to contain large-scale errors of $\sim$10%–20%. We applied the "correction flat" of Phillips et al. to each pipeline-calibrated image to remove the large-scale flat-fielding errors, as well as some odd/even pattern introduced by the pipeline flat. On the basis of large-aperture photometry performed on a spatially median-filtered image (to avoid cosmic-ray contamination), we then selected all galaxies with $I_{785} \leq 20.6$. We chose this magnitude cutoff so that structural information, namely, length scales, could be reliably obtained, though many galaxies fainter than this limit are visible. Also, at these magnitudes it is relatively easy to separate stars and galaxies by visual inspection: stellar images have sharp cores; they are not as extended; and (except near our magnitude limit) they show the sharp "tendrils" of the PSF.

TABLE 1

OBSERVATIONS

Field (1)	Date (2)	R.A. (3)	Dec. (4)	l^{II} (5)	b^{II} (6)	N(I) (7)	Expo. (8)	Area (9)	# gal. (10)
MDSW1	1992-Jan-6–8	12:29	+02.2	290	64.5	8	18244	5.7	6
MDSW2	1992-May-11,13	13:12[a]	+42.6[a]	109	74.0	2(4)	1950[b]	7.8	18
MDSW3	1992-May-21	10:04	+29.0	200	53.3	1	2400	5.7	23
MDSW5	1992-Jun-5	15:03	+66.2	105	46.0	2	4800	5.7	5
MDSW10	1992-Jul-25	02:29	−10.2	181	−61.6	1	1800	5.7	15
MDSW11	1992-Jul-28	23:05	+03.1	78	−50.3	1	1800	5.7	6
MDSW12	1992-Aug-8	22:17[a]	+00.2[a]	63	−44.0	1	1800	5.7	6
MDSW15	1992-Sep-26	20:05	−55.8	342	−32.3	1	2400	5.7	16
MDSW16	1992-Sep-30	02:18	+01.7	162	−54.5	1	1800	5.7	5

NOTE.—Cols. (1) MDS field number; W = WFC. (2) Date of observation. (3) and (4) Approximate celestial coordinates for MDS field (J2000). (5) and (6) Galactic coordinates for MDS field. (7) Total number of F785LP frames used (in field MDSW2, some galaxies were examined on four frames). (8) Total F785LP exposure time (seconds). (9) Effective area covered by our sample (arcmin^2). (10) Number of galaxies selected.

[a] Dithered field.

[b] Average of 1800 and 2100 s (additional exposures were 2100 s).

2.2. *Reduction of Selected Images*

We extracted subrasters (typically 128 pixels square) around the selected galaxies and removed cosmic-ray events, first using an automated procedure based on photon statistics and "sharpness" of the events (Phillips 1993), and finally by visual inspection. Special care was taken near the cores of object images. For multiple exposures with little or no spatial shift, the individual exposures were co-added using the STSDAS IMCOMBINE task[4] with an appropriate noise model to remove cosmic-ray events. For the dithered fields (W2 and W12), we have analyzed a few individual images that contain the most galaxies, rather than attempting to combine the offset images with the attendant problems of geometrical distortions and variable PSFs.

Noise severely affects the restoration of low-S/N images. Prior to deconvolution, we used the procedure described in the Appendix to estimate the noise pattern in each image, essentially by enforcing positivity (above the sky level) through many iterations of the standard Lucy-Richardson algorithm. Basically, this procedure identifies as noise any structure which is inconsistent with real signal degraded by the PSF. The procedure reduces noise by about an order of magnitude in the low-S/N regions, although it leaves the stronger noise spikes in regions where there is significant flux from the galaxies. Simulations with model galaxies (see the Appendix) show that the procedure provides a real advantage in measuring scale lengths. Each "noise-reduced" galaxy image was then deconvolved through 25 iterations of the Lucy-Richardson algorithm, using model PSFs generated with TINYTIM, Version 2.1 (Krist 1992). While the model PSFs are known *not* to reproduce actual PSFs perfectly (see Elson, Forbes, & Gilmore 1994; Baxter et al. 1993), they are the only feasible option in many high-latitude fields due to the scarcity of field stars, and they appear to do an adequate job of restoring *large-scale* structures.

The relatively small number of iterations was chosen as a compromise between restoration of sharp features and refraining from "overresolving" the noise. Lauer et al. (1992) have shown that, after 20 iterations of the Lucy-Richardson algorithm, the galaxy profile for a high-S/N elliptical is restored to within 1% for radii beyond 0.″2, or two WFC pixels. Since we use the Lucy-Richardson algorithm in its linear form, the same rate of convergence found by Lauer et al. should apply to our lower S/N cases. This finding, as well as the tests with simulated data discussed in the Appendix, gives us confidence that the deconvolved galaxy profiles beyond the innermost 2 pixels are adequately restored for the purposes of determining large-scale structural parameters such as disk scale lengths. However, small-scale features are often not well restored, and noise spikes often taken on the appearance of real small-scale structure. Figure 1 (Plate 1) shows some representative subrasters at three different stages in the reduction process: the pipeline-calibrated (and flat-field corrected) data, after cosmic-ray cleaning, and after deconvolution. Finally, another deconvolved image of the same object but from a different CCD is shown for comparison. These are all from the (dithered) W2 field, and the first two galaxies shown are among the brightest in the sample. It is immediately obvious that cosmic-ray events and noise both pose serious problems in working with these data. A detailed comparison between the two deconvolved images shows that very few of the weaker small-scale features match, and therefore such features are almost certainly artifacts of the noise. However, each pair of deconvolved images is immediately recognizable as being of the same galaxy, and larger scale structures match quite well. Along with our tests on model galaxies (§ 4.2 and Appendix § A.2), these results give us confidence that our morphological estimates are not severely compromised by uncertainties in the deconvolution process.

3. PHOTOMETRIC AND MODEL-INDEPENDENT STRUCTURAL PARAMETERS

Photometry has been carried out for our galaxy sample on both the processed, cosmic-ray–cleaned ("observed") frames and the noise-reduced, deconvolved image subrasters described above. Identical photometric techniques were used for both. The deconvolved images were analyzed to derive model-independent measures of size and apparent brightness. In this study we present half-light radii ($r_{1/2}$) and total I_{785} magnitudes as defined below. Photometry on both the observed and deconvolved images allows us to check in quantitative detail whether the deconvolutions conserve flux for each object (as opposed to, e.g., the entire image). In the follow-

[4] Ratnatunga et al. (1994) have found that this task does not weight the input images properly in all cases; however, since all of our images were of comparable exposure, this is not a problem for our data.

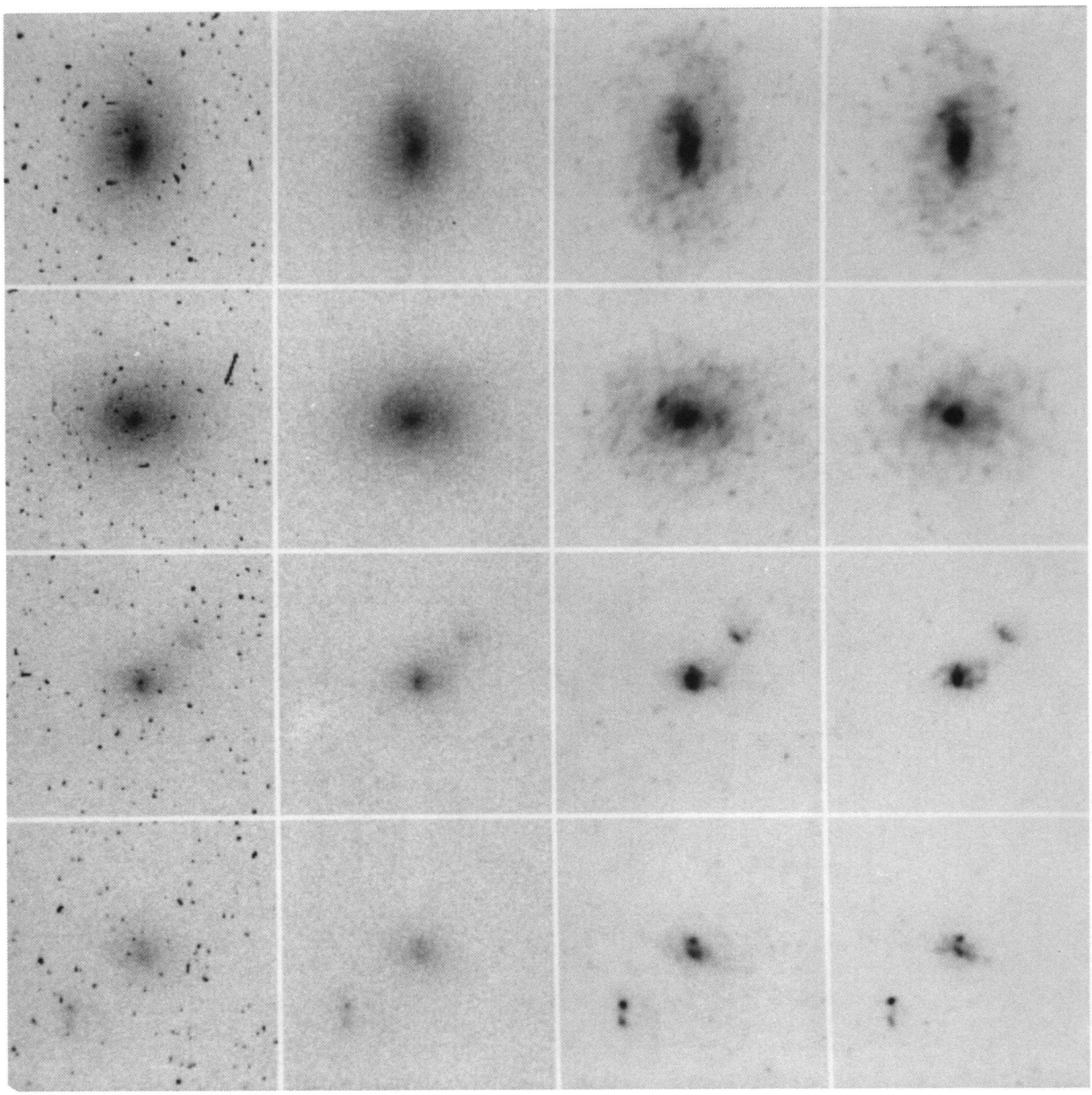

FIG. 1.—Various stages of the reduction process for four galaxies from the "dithered" MDSW2 field. From left to right, the images have been pipeline processed, cosmic-ray cleaned, and deconvolved (following the subtraction of an estimated noise field). The rightmost panel shows a deconvolution of the same galaxy, but from an image on another CCD chip, in order to show the effects of different noise patterns *and* different PSFs. Large-scale structures match well, but the weaker small-scale features appear to be artifacts of the noise. The four galaxies shown (top to bottom) are W2-1, W2-6, W2-7, and W2-8.

PHILLIPS et al. (see 444, 23)

ing subsections we briefly describe the photometric procedure and assess the random and systematic errors.

3.1. *Multiaperture Photometry*

Multiaperture photometry was performed with software built around IRAF's APPHOT.PHOT routine. For different circular apertures between 1 and 80 pixels (0".1–8".0) in radius were chosen. For such faint objects, however, an accurate determination of the sky background level is crucial, and so particular attention was paid to this problem.

Contamination by nearby galaxies poses a serious problem for accurate galaxy photometry. Additional software has been developed by one of us (M. A. B.) to iteratively blank out neighboring objects when calculating sums and areas in circular apertures with APPHOT.PHOT, as well as all objects when determining the sky mean and mode. Blanking radii were set conservatively to 5" (radius) for all primary objects, and 3" for neighboring objects, with the added stipulation that the blanking radii of neighboring objects must be less than half the distance to the primary object. This value of the blanking radius was determined from visual inspection of the curves of growth of the encircled light from an initial pass of the photometry using 3" blanking radii for all objects. (Automated iterative schemes for determining blanking radii are possible and will be discussed elsewhere.) In addition to blanking out neighboring objects, bad pixels were replaced with the average of the pixel value in the appropriate annulus. Our software provides the flexibility to set the sky level to either the global mean or mode on the image subraster, or the local mean in any annulus about each object (where all quantities are calculated with objects blanked from the image). The photometry discussed here uses a global mean determined for each subraster for sky. Tests show that there is very little difference between using a global mean or mode, pointing to the efficacy of blanking out all detected objects, as well as indicating that cosmic rays have been removed well.

3.2. *Calibration*

Chip-to-chip renormalizations and the single F785LP photometric zero point were adopted from the Appendix of Phillips et al. (1994). The current flat-field corrections from Phillips et al. reduce systematic errors to roughly ± 0.02 mag across the full field of the WFC. While this is already a substantial improvement over the original systematic errors of ~ 0.1 mag, this uncertainty may be further reduced in the future with better flat-fielding and/or calibration photometry.

The magnitudes discussed here are instrumental and have not been converted to any standard system (e.g., Johnson or Kron-Cousins). The I_{785} magnitude is quite similar to Cousins I magnitude (I_C); transformations for stellar photometry are given in Harris et al. (1991), and the difference $I_C - I_{785}$ is only ~ 0.1–0.2 for colors typical of galaxies at redshifts less than 0.5.

3.3. *Total Magnitudes and Half-Light Radii*

The definition of total magnitude for galaxies is difficult because galaxies have different shapes and sizes. The choice of a photometric aperture requires a trade-off between reliability (S/N and systematic errors in the background) and the actual fraction of the total light measured. Hence, most non–profile-fitting methods used to determine total magnitude for faint galaxies do not measure all of the flux. Photometric methods which are independent of galaxy isophote typically measure $\sim 80\%$–90% of the total light (Kron 1980; Infante 1987). This percentage can depend on profile shape, particularly if galaxies are well resolved (Bershady et al. 1994). In the case of FOCAS, which uses an isophotally derived photometric aperture, the percentage can be much smaller and highly redshift dependent (Jarvis & Tyson 1981). Profile-fitting methods used to determine total magnitudes (e.g., Dressler & Gunn 1992) can be optimal in the S/N sense, but will be subject to systematic errors if the template profiles do not well represent the images being measured. Since one aspect of our program already involves fitting standard bulge/disk model profiles, we chose to carry out our total magnitude and $r_{1/2}$ determinations in a nonparametric (model-independent) way, using aperture photometry and growth curves.

Our choice of aperture is driven by two considerations. First, our galaxy images have relatively high S/N for faint galaxy photometry. Second, these total magnitudes are to be used to (1) determine half-light radii and (2) estimate disk-to-total ratios (see § 4.2). Based on these considerations, the total magnitudes have been designed to include a fraction of light that is close to total, and to be unaffected by systematics due to different galaxy shapes and sizes at the level of our random errors. We do this empirically by examining the curves of growth for the ensemble of galaxies in the raw and deconvolved images with the criterion that S/N can be reduced in exchange for including more light. As seen in Figure 2, apertures of radius 5".2 are sufficiently large so as to enclose nearly all the light in even the largest galaxies for both observed and deconvolved images. Although smaller apertures could be used for some galaxies without losing significant amounts of light (and thereby gaining S/N). the tailoring of apertures to individual galaxies can be prone to profile-dependent systematics, especially since the deconvolved images contain resolved light profiles. Thus, photometry within a fixed 5".2 radius aperture is adopted here for total magnitudes. The half-light radus, $r_{1/2}$, is derived by interpolating in the curve of growth to determine the radius at which half of the total light is enclosed.

3.4. *Estimated Random Errors*

Since multiple frames were not photometered for each object, magnitude errors are estimated from the quadrature sum of the measured shot noise in the sky background (in the aperture size used for the object), the square root of the object flux *as determined in the observed image* cleaned of cosmic rays, and the zero-point uncertainty (see § 3.2). The random error in the determination of the sky level is negligible ($\lesssim 0.5\%$) because of the large effective aperture. The estimated errors from the observed images are adopted because the sky background in the deconvolved images is correlated so that the standard deviation of the background does not represent the noise in the usual way. Magnitude errors are defined to be the positive root of the error function (e.g., Koo 1986). Characteristic errors are ± 0.04 mag at $I_{785} = 20$. As a check on the estimated errors, we examined five galaxies in the dithered W2 field for which multiple observations were available. The measured standard deviations in Table 2 are comparable to the estimated errors for the same object in Table 3.

Formal error estimates for $r_{1/2}$, calculated from the estimated errors in the curve of growth, are between 2%–4% for the observed images, and 0.5%–2% for the deconvolved images. The smaller estimated errors for the deconvolved images are again a reflection of the correlation of pixel values in the sky background in the deconvolved images. However, these formal errors in the observed images appear to be an

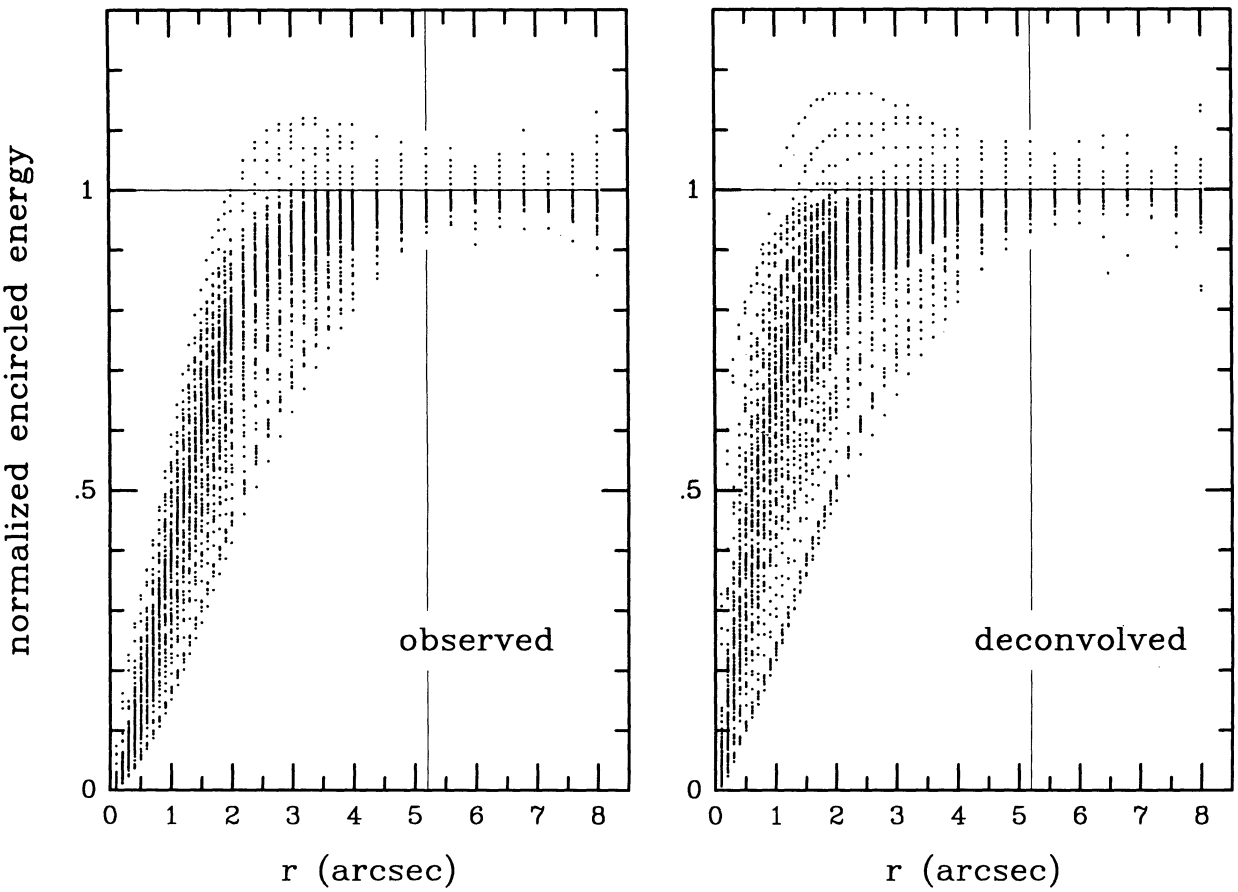

FIG. 2.—Encircled energy vs. circular aperture radius for our galaxy sample. The curves of growth have been normalized between $4''.8 < r < 8''$. The broken vertical line drawn at radius $5''.2$ corresponds to the adopted aperture for total magnitudes. The solid horizontal line at unity is for reference.

underestimate of the true uncertainty. They are smaller, for example, than the measured standard deviations for the five galaxies in W2 with multiple measurements (Table 2). On the basis of these five galaxies we estimate that the deconvolved $r_{1/2}$ have uncertainties nearer to $\sim 5\%$.

3.5. *Systematic Errors*

Systematic errors in the determination of the mean sky level occur because of contamination from object flux. Using the mode instead of the mean does not eliminate this problem and can lead to other difficulties as a result of the way the mode algorithms are typically implemented (e.g., from improperly binned data, or A/D converter problems). On average, the growth curves in Figure 2 turn down very slightly at large radii. This behavior is similar for both observed and deconvolved images. Assuming that all of the object flux is enclosed within a radius of $5''.2$, the flux measured between $5''.2$ and $8''.0$ divided by this annular area provides an estimate of the error in the measured sky level. The difference between $5''.2$ and $8''.0$ aperture magnitudes is -0.008 mag (median), or -0.006 ± 0.051 mag (mean), for the observed images and -0.005 mag (median), or -0.005 ± 0.049 mag (mean and standard deviation), for the deconvolved images. For magnitudes measured within a $5''.2$ radius aperture, this corresponds to an error of -0.009 mag (median), or -0.009 ± 0.065 mag (mean), for the observed images and -0.005 mag (median), or -0.007 ± 0.063 (mean), for the deconvolved images. This is qualitatively consistent with the error in the sky level being caused by contamination from the wings of the object profiles; in the deconvolved images the object profiles are more compact. However, the amplitude of this small (less than 1%) systematic effect is not statistically significant, and we therefore have made no correction to the total magnitudes. In fact, the flatness of the growth curves at large radii in Figure 2 are testament to the accuracy of our sky determination. As mentioned in § 3.2, there may be some residual systematic errors due to imperfect field flattening, but these are at levels below 2%.

3.5.1. *Observed versus Deconvolved Measurements of Observed Data*

It is very reassuring to find that total magnitudes are little affected by the deconvolution process. The mean difference between observed and deconvolved total magnitudes is -0.03 mag (± 0.08 dispersion), and the median difference is zero, as illustrated in Figure 3. The offset between the mean and the median is largely driven by the tail of objects at negative magnitude differences (less than -0.08 mag). If an iterative clipping algorithm (10 iterations with a 3 σ clip) is applied to the distribution of magnitude differences, the mean difference becomes 0.00 mag (± 0.02), consistent with visual inspection of the central peak in the histogram in Figure 3. It is interesting to note that all of the objects with large magnitude differences (observed − deconvolved < -0.08 mag) have close companions or neighbors. This is consistent with the aperture photo-

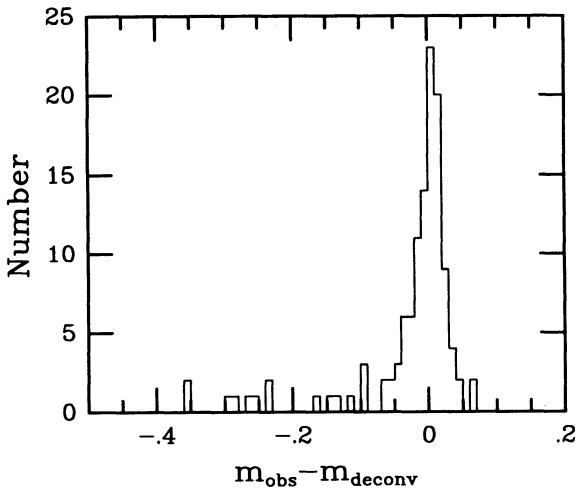

FIG. 3.—Histogram of the differences between the observed and deconvolved magnitudes as measured within the same 5″2 radius aperture.

metry on the observed images being more contaminated by flux of neighboring objects than photometry on the deconvolved images, because of the large halos from the aberrated PSFs.

As expected, we find the deconvolved $r_{1/2}$ to be significantly smaller than the observed values. The ratio of the deconvolved to observed $r_{1/2}$ is 0.56 (median), or 0.57 ± 0.15 (mean), and of course is strongly correlated with galaxy size, as seen in Figure 4. Half-light radii for objects with deconvolved $r_{1/2} >$ 1″5 are changed by less than 20% by the deconvolution process, whereas objects with deconvolved $r_{1/2} < 0''.5$ are changed by more than a factor of 3. Although this behavior is qualitatively consistent with expectations, models are required to ascertain whether the change in $r_{1/2}$ due to deconvolution is quantitatively correct. Such models are considered next.

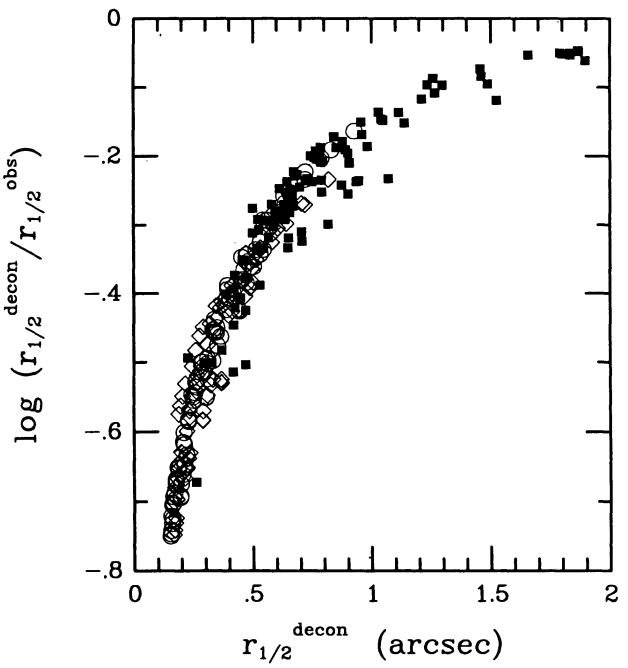

FIG. 4.—Ratios of the deconvolved to observed half-light radii are plotted vs. the deconvolved half-light radius. Solid squares represent observed data; open diamonds represent model data at S/N smaller than the observed data; open circles represent model data at S/N typical of the observed data. For the model data, the "observed" half-light radii refer to values measured on the convolved model images as defined in § 3.5.1. The model data do not span the full range of sizes in the observed data, but the trends of the two distributions are in good agreement.

3.5.2. *Intrinsic versus Deconvolved Measurements of Model Data*

For the tests described here, we use the full set of the simulated galaxy models described in Appendix § A.2. Two S/N levels are considered: the single-orbit-exposure equivalents to $I_{785} \sim 19.6$ mag and the $I_{785} \sim 21.6$ mag case. Note that the latter case is about 1 mag below the faint magnitude cutoff in our actual sample and that the former case is more representative of the bulk of our sample. Using these model galaxy images, we have compared the effects of deconvolution on the measured $r_{1/2}$ as follows. The galaxy models are first convolved with the WFC PSF, and the noise is added to these images; these data are referred to as the "convolved model images." The convolved model images are then deconvolved in the same way as the real data; these data are referred to as the "deconvolved model images." The change in the measured $r_{1/2}$ between the convolved and deconvolved model images is analogous to the change between observed and deconvolved real images. Figure 4 shows that the ratio of convolved to deconvolved model $r_{1/2}$ has an identical correlation with deconvolved model $r_{1/2}$ as do the real data (i.e., observed-to-deconvolved $r_{1/2}$ vs. deconvolved $r_{1/2}$).

Next, we have compared the original model $r_{1/2}$ with the deconvolved model $r_{1/2}$ for the two simulated S/N cases, shown in Figure 5*a*. Although the ratio of deconvolved to original model $r_{1/2}$ is correlated with size, the mean difference between the two is quite small, being only +0.02 for both the high- and low-S/N cases, and with dispersions of 0.03 and 0.05 mag, respectively.

It is worthwhile to examine the systematic dependence of the deconvolved model $r_{1/2}$ on other model parameters, such as disk-to-total ratio (D/T) and disk inclination, as illustrated in Figures 5*b* and 5*c*. As D/T changes, we find that systematic trends in $r_{1/2}$ are the same in the mean but that the scatter becomes larger with more disk-dominated systems. In contrast, there is a small systematic change in the mean with inclination, but the scatter at any given inclination is roughly the same. This means that in principle we could reduce the scatter in this plot by a factor of 2 by making an inclination correction to the deconvolved model $r_{1/2}$. However, to do so for the real data would require (1) an accurate measurement of galaxy ellipticity, and (2) a way to transform the apparent ellipticity into inclination. Since the latter step requires knowledge of the D/T as well as the assumption that a pure disk + bulge model accurately describes real galaxies, we have not attempted to make such a correction, especially given the low level of systematic effects inferred from the models.

In summary, there is only a small level of systematic bias in the deconvolved model $r_{1/2}$. Given that the change of $r_{1/2}$ between observed and deconvolved images has the same behavior with size for both model and real data, it is reasonable to conclude that the systematic errors for $r_{1/2}$ of the real data are also small.

4. MODEL-DEPENDENT STRUCTURAL PARAMETERS

4.1. *Method*

To measure structural parameters of the galaxies, we fit the two-dimensional light distribution of the deconvolved images

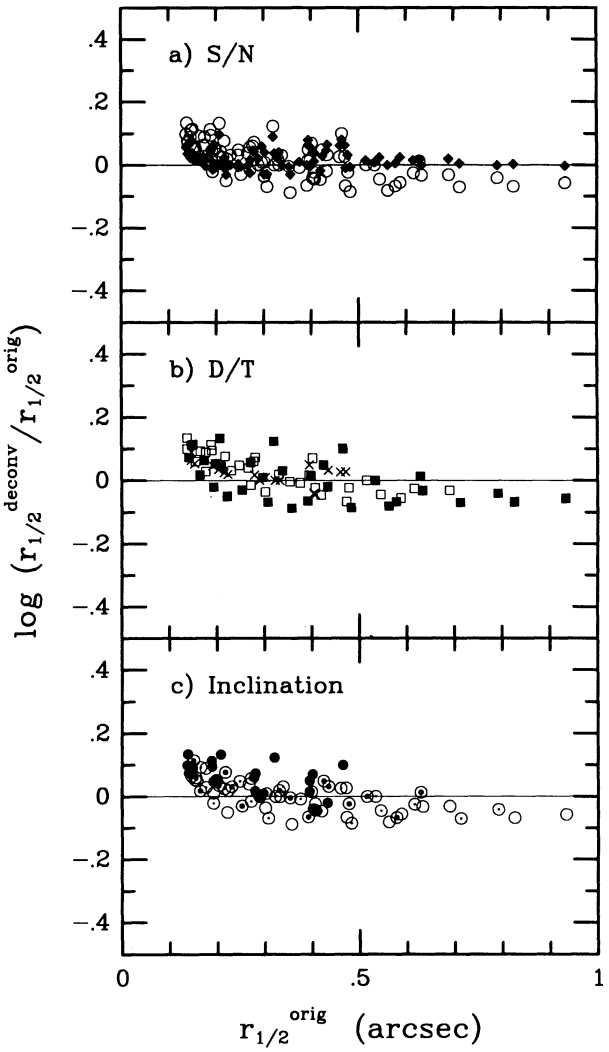

FIG. 5.—Ratios of the deconvolved to orginal model half-light radii are plotted vs. the original model half-light radius, where "original model" refers to the model data prior to convolution, noise degradation, and subsequent deconvolution. (*a*) Open circles represent model data at S/N typical of the observed data; solid diamonds represent model data at S/N smaller than the observed data. Panels (*b*) and (*c*) are similar, but use the low-S/N models only, and demonstrate systematic errors which correlate with model galaxy parameters. (*b*) Systematic errors with D/T; symbols denote bulge-dominated (×), D/T of 0 and 0.18; disk-dominated (*filled boxes*), D/T of 0.85 and 1; and intermediate cases (*open boxes*), D/T of 0.43 and 0.62. (*c*) Systematic errors with inclination; symbols denote major-to-minor axis ratios b/a of 1 (*open*), 0.7 (*small dot*), 0.4 (*large dot*), and 0.1 (*filled*). From (*b*) and (*c*), we see that systematic errors are present, but they are small (generally less than ~10%) for most galaxy model parameters.

with elliptical isophotes, in effect producing an azimuthally averaged profile; this is then used to estimate the structural parameters. The ellipse fitting is done with the STSDAS ISOPHOTE package, which outputs isophote intensity and ellipse parameters as a function of radius (see Forbes & Thomson 1992 for more details of the package).We start with an estimate of the galaxy center, ellipticity, and position angle, and then these parameters are allowed to vary throughout the ellipse-fitting process. The fitting task uses the median value around each fitted ellipse so as to form a smooth model relatively unaffected by fine structural features within the galaxy image—whether real or artificial (see the Appendix). The sky value is taken to be the same as that used for image deconvolution. The resulting surface brightness profile is then fit, as a function of the semimajor axis, with a multicomponent $r^{1/4}$-law and exponential disk profile using the STSDAS task NFIT1D. In particular, the bulge is fit with

$$I(r) = I_e \exp\left[-7.67(r/r_e)^{1/4} - 1\right],$$

where I is the surface brightness, r_e is the half-light radius, and $I_e = I(r_e)$. The disk component is fit with

$$I(r) = I_0 \exp\left(-r/r_d\right),$$

where r_d is the disk scale length and I_0 the central surface brightness. In general, we fit galaxies with these two profiles simultaneously to avoid the systematic bias that would be introduced if only one component were fit at a time. We make no attempt to fit the profiles of galaxies showing highly distorted or multiple-nuclei structure.

The profiles are fit between an inner radius of 2 pixels and an outer radius usually determined by the ellipse-fitting task, typically ~25–30 pixels. Our tests involving the simulated galaxy models (discussed below) suggest that more reliable results are obtained by limiting the inner radius to 2 pixels rather than by fitting into the very center. The outer radius represents the point at which the ellipse-fitting program no longer returns a new ellipse solution, indicating the program has difficulty separating the galaxy from background light. In a few cases, the outer radius was extended or truncated to be within the range 1.5–5 times $r_{1/2}$, thereby ensuring that the disk was fit over a reasonable number of scale lengths.

Although our method for deriving scale lengths is similar to that used by others for nearby galaxies, there are several caveats to keep in mind. Ellipses are approximations to the real structure that work well for most early-type galaxies (i.e., E–Sa), but clearly become poorer estimates for disk systems with strong spiral arms or bars, or late-type dwarf galaxies. When fitting the profiles, we assume that all galaxies can be decomposed into a combination of $r^{1/4}$-law bulges and exponential disks. However, fits of this type may not be unique; i.e., different sets of bulge and disk prameters can give comparably good fits (in a formal sense) to the same data. This seems to be particularly true when there is a prominent (or dominant) bulge. Furthermore, fits with these two models are often only simplistic approximations, unable to accommodate features such as bars; and even normal, nearby disk galaxies frequently cannot be satisfactorily decomposed into simple disk and bulge components (e.g., Kent 1985).

4.2. *Testing the Profile-fitting Procedure*

Within the goal of minimizing errors in our derived structural parameters, we have two main purposes for testing the procedure against model galaxies. The first is to test the reliability of the fitting procedure itself. This is a concern since the small angular size of the sample galaxies combined with the WFC pixel scale means that the galaxies frequently show rather steep gradients as well as undersampled cores (see Windhorst et al. 1994). We perform this test by making measurements of ideal model galaxies (before any PSF dergradation) of similar size to our sample and comparing the results to the known input model values. The second purpose is to test the reliability of measurements from deconvolved images, by comparing them against the measurements of the "original model" (predegradation) images (as distinct from the known input model values). This affords a check on the deconvolution pro-

cedure free of any biases introduced by the fitting method. Several similar tests are shown in the Appendix.

For the following tests, we adopt a subset of the galaxy models described in the Appendix. We have chosen two sets of model galaxies with scale lengths of 0".26 and 0".64. We will see below (§ 5) that these values bracket the minimum and median values in our sample galaxies. Both sets include two S/N regimes: the single-orbit-exposure equivalents to $I_{785} \sim 19.6$ (high-S/N case) and $I_{785} \sim 21.6$ (low-S/N case). Recall that the low-S/N case is about ~ 1 mag below the faint magnitude cutoff in our actual sample, whereas the high-S/N case is more representative of the typical sample galaxy. Again, these magnitudes will be seen to bracket the minimum and median values in our sample. For both larger and brighter galaxies, undersampling and biases introduced by deconvolution are less problematic. The models range from bulge-dominated to disk dominated; the disk inclination is 45° for all.

We have fit the model galaxies following the method described above. We find that our measured bulge r_e values are sytematically underestimated, sometimes by large factors. Although in principle a correction factor could be determined and applied, we have instead deemed the effective radii derived from profile fitting to be unreliable, and so measured effective radii will not be used in the analysis of our real galaxy data. The results for disk scale lengths are more encouraging, as seen in Figure 6. First, we note that the disk scale lengths measured in the original model images agree quite well with the known model values, shown by the vertical arrows. Thus, the ellipse- and profile-fitting procedures appear reliable for disk scale lengths. Furthermore, the measured disk scale lengths in the deconvolved model galaxies are in quite good agreement with the known model values, particularly in the higher S/N case where the dispersion is $\sim 10\%$. In the low-S/N regime, the dispersion has only increased to $\sim 20\%$.

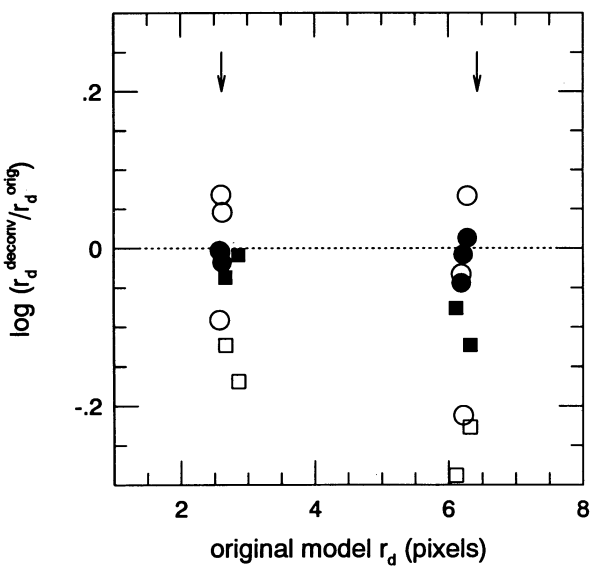

FIG. 6.—Measured disk scale lengths for a subset of simulated galaxy models. The input original model values are indicated by the two arrows. The circles represent disk-dominated models, and the squares bulge-dominated models. The higher S/N models are filled, and the lower S/N cases are open symbols. This figure indicates that the procedure for measuring disk scale lengths is valid (i.e., original model scale lengths are close to the input value) and that disk scale lengths can be recovered from deconvolved images to within $\sim 20\%$ for most of the galaxies in our observed sample.

4.3. *Disk-to-Total Ratios*

In addition to length scales, the relative contributions of the disk and bulge to the total light of the galaxy provide valuable morphological information. Determining the bulge-to-disk ratio is difficult, however, because it depends not only on the characteristic length scales and surface brightness but also on the intrinsic ellipticities and inclinations. In principle, a full two-dimensional fit is necessary to solve for all of the relevant parameters. Even then disk features such as bars, rings, and strong spiral arms can make it very difficult to get a satisfactory decomposition.

Further difficulties are encountered when using deconvolved images. For example, the cores of bulges are not well restored with a small number of deconvolution iterations, yet this is the only high-S/N regime where bulge light will dominate over disk light in most disk galaxies. Also, unrestored flux tends to have radial symmetry, which will bias the ellipticity of isophotes—particularly the outer isophotes where most information about disk ellipticity is to be found. Given these many problems, it may seem unlikely that useful bulge-to-disk information can be extracted from our images. However, visual inspection shows a clear difference between bulge- and disk-dominated systems, as do the major-axis profile fits. This suggests that some approach should be possible that provides a quantitative estimate of the bulge-to-disk ratio, even if the results cannot be established with fine gradation.

Considering the problems just discussed, a full two-dimensional fit is not merited. On the other hand, a major-axis profile fit is only useful for bulge-to-disk measurements if we have some knowledge of the correct ellipticities of the disk and bulge. If these are not available, another approach would be to measure the profile along an axis chosen to remove the projection effects of the disk, and to assume that the bulge has either spherical symmetry or the same ellipticity as the disk. In this case, the total disk light is calculated as

$$D = 2\pi I_0 r_d^2 = 2\pi I_0 ab ,$$

where a and b are the major- and minor-axis scale lengths and r_d is the scale length measured along an axis chosen so that $r_d = (ab)^{1/2}$. This axis varies from $\sim 45°$ with respect to the major axis for nearly face-on disks, to 0° for the limiting case of an edge-on disk. Again, however, we need to know the true ratio of a/b, which is usually determined from the outer isophotes but which we know is biased in the deconvolved images.

We have adopted a simplified version of this last approach—we measure the scale length along a *fixed* axis at 34° with respect to the major axis. This is the mean of the correct angle averaged over all inclinations; it is near the optimum angle for the median disk inclination; and it is only 11° from the optimum angle for a virtually face-on disk. Using this fixed angle results in less than 10% error in the projected area of a circular disk for all disk inclinations less than 70°. Disks with inclinations greater than this are likely to suffer severe internal absorption, and so should be excluded anyway; fortunately, these nearly edge-on systems are easily identified and can be isolated from the sample. Since we know the bulge profiles are suspect, we derive the disk-to-total ratio (D/T) rather than directly measuring a bulge-to-disk ratio. The disk light is estimated from the surface brightness profile along the 34°-axis and compared to the total magnitude from the aperture photometry (§ 3.3).

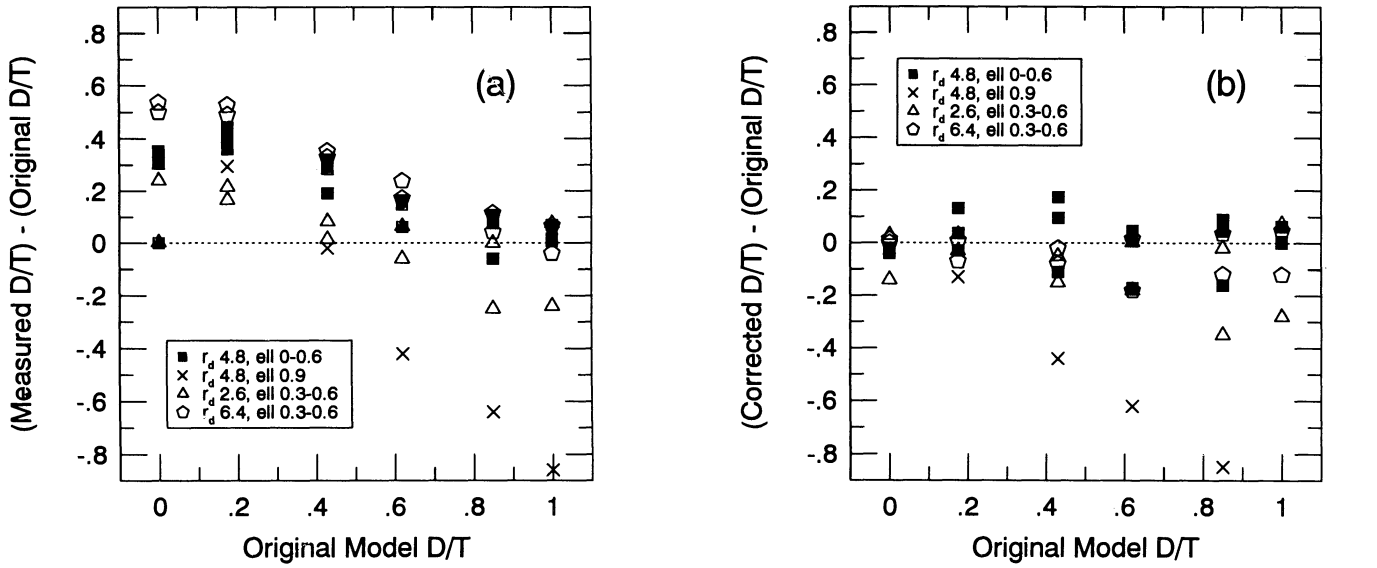

FIG. 7.—(*a*) Disk-to-total ratios (D/T) measured for deconvolved model images; the models span a range of galaxy parameters. There are strong deviations below $D/T \sim 0.7$, systematic with input model D/T, galaxy size, and inclination. The very highly inclined models (×) show the deviation expected from using our procedure for measuring D/T. Edge-on galaxies are easily identifiable and excluded from analysis. (*b*) Same as (*a*), but with an empirical correction applied to the measured D/T values. While the scatter remains large, the systematic errors are much reduced (excluding the expected large deviations in the nearly edge-on cases) and are now $\lesssim 0.1$.

Once again, we can test this approach using the model galaxies. Figure 7*a* shows the results for a subset of the models, spanning a range in disk inclinations and disk scale lengths. We plot the error in measured D/T against the known original model D/T. The nearly edge-on case is badly in error, but at this inclination the projected area of the disk (and hence the disk luminosity) is expected to be underestimated by about a factor of 3. The other three disk inclinations should have projected areas well approximated by using the 34°-axis. Examining these cases, we find reasonable agreement for larger values of D/T. Below $D/T \sim 0.7$, however, the measured values start to deviate significantly. The amount of deviation depends both on disk inclination and disk scale length, as well as on the true D/T. We have derived an approximate empirical correction for these systematic biases; the results following this correction are shown in Figure 7*b*. It should be noted, however, that the corrections are as large as the scatter over much of the range, and so will not be correct in detail (i.e., for a single galaxy) but only statistically correct for a large sample.

4.4. *Stability of Results in Observed Images*

It is important to quantify both the random and systematic errors for our sample galaxies. While useful information (especially about systematic errors) comes from tests with simulated data, *real* data will contain many additional sources of uncertainty, including the effects of cosmic-ray removal, S/N variations, and inaccuracies in the simulated PSF used for image deconvolution. An insight into the errors associated with the first two sources can be gained from our multiorbit observations with the same pointing. We selected a single 2400 s exposure from the set of eight images in the first field (MDSW1) and determind major-axis scale lengths in the usual way. The measured scale lengths were then compared to the measurements of the same five galaxies from the combined image of eight co-added frames with a total exposure of 18,244 s. The single frame has an exposure time typical of the single-orbit images in our sample and thus provides an independent test of the effects of both lower S/N (factor of 2.7) and cosmic-ray removal in a single frame. Figure 8 shows the comparison between scale lengths derived from the single frame and those from the combined frames. The disk scale length measurements are in reasonable agreement (~15% rms). This gives us confidence that single frames can return reliable scale lengths even though they are of lower effective S/N and cosmic-ray removal is more problematic.

A further issue, noted previously, concerns how accurately the simulated PSFs reproduce the true PSF and the effect that

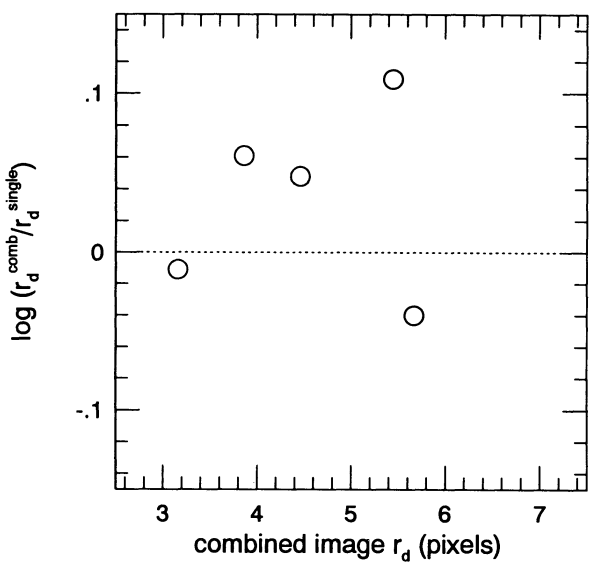

FIG. 8.—Disk scale lengths for five galaxies in the MDSW1 field. Scale lengths are measured for the same galaxies on a single exposure (2400 s) and compared to those from the combined image of eight exposures (18,244 s). This figure shows that single orbit exposures (i.e., with lower S/N and increased cosmic-ray contamination) give comparable disk scale lengths to multi-orbit fields to within ~15% rms.

any discrepancy has on image deconvolution and on the derived structural parameters. An empirical indication of the effects of the spatially variable PSF can be gained by comparing several images of the same galaxy in multiorbit dithered fields. These galaxies will be imaged in different parts of the same or different CCD chips, and so the individual galaxy images will have different PSFs. A comparison of the measured scale lengths will provide information about the combined effects of the PSF and image deconvolution. As in § 3.4, we examine the five galaxies that appear on four different frames of the W2 field. Their measured disk scale lengths and D/T ratios are summarized in Table 2. These galaxies span the range of scale lengths and magnitudes found for our entire sample and thus should be representative. As seen in the table, scale length measurements from different frames agree reasonably well, to within typically 5%–10%, with a maximum dispersion of 20% in the faintest case. The D/T measurements also show good agreement.

5. RESULTS

The measured photometric and structural parameters for the galaxies are listed in Table 3. A total of 100 galaxies are included, and of these, 90 have measured model-dependent structural parameters (disk scale lengths and/or $r^{1/4}$-law effective radii). This table forms the database for our quantitative analysis. Column (1) gives the galaxy identification, in the form of field number followed by sequence number within the field (e.g., W3-2 is the second galaxy examined in field MDSW3). Columns (2) and (3) give the location of the center of the galaxy. Columns (4) and (5) give I_{785} measured in the restored image within a circular aperture of radius 5.″2, and the estimated error in this magnitude based on the quadrature sum of the formal measurement error, a flat-fielding error of 2% (internal to the individual CCD), and a 1.2% error for chip-to-chip normalization (see Phillips et al. 1994). Column (6) lists $r_{1/2}$, the radius in arcseconds which contains half the light measured in the 5.″2 radius aperture as calculated from the photometric curve of growth. Errors in $r_{1/2}$ are expected to be $\lesssim 5\%$ (§ 3.4). Columns (7) and (8) give the exponential disk scale length from the simultaneous bulge and disk fit to the major-axis profile, and the error provided by the fitting procedure. Measured D/T values, based on the off-axis profile fit (disk component) and photometry (total light), are listed in column (9); these are known to be systematically overestimated (see § 4.3) and are unreliable for nearly edge-on objects. Column (10) gives the location of the image in the "atlas," Figures 9 and 10 (Plates 2–4 and 5–7). Finally, column (11) lists comments about the individual objects.

Three bright stellar objects are also included at the end of Table 3. They were measured for comparison with the galaxy parameters, and it is reassuring that the measured $r_{1/2}$ in each case is significantly smaller than for any of the galaxies except W15-9 and that no evidence for a disk was found by the profile-fitting procedure. Inspection of the unrestored image of W15-9 confirms that it is not a (simple) stellar image, but the deconvolved image reveals that it is almost certainly a star superposed on the edge of a faint galaxy, with most of the flux belonging to the star. (As the galaxy is probably fainter than our magnitude limit, it will be excluded from the analysis below.)

Figures 9 and 10 show a montage of unrestored and deconvolved images for the sample galaxies, ordered by disk-through bulge-dominated systems. Edge-on galaxies, for which the D/T ratio could not be measured, are grouped at the end, followed by galaxies which could not be satisfactorily fit by the profile-fitting procedure.

TABLE 2

COMPARISON OF MDSW2 GALAXY MEASUREMENTS

Galaxy (1)	N (2)	I_{785} (3)	$r_{1/2}$ (4)	r_d (5)	D/T (6)
MDSW2-1	4	17.74 ± 0.05	1.74 ± 0.02	1.23 ± 0.08	0.87 ± 0.05
MDSW2-6	4	17.71 ± 0.01	1.79 ± 0.04	1.42 ± 0.05	0.96 ± 0.06
MDSW2-7	3	19.56 ± 0.06	0.70 ± 0.03	0.45 ± 0.04	0.91 ± 0.04
MDSW2-8	4	20.09 ± 0.04	0.77 ± 0.06	0.48 ± 0.02	0.95 ± 0.05
MDSW2-9	4	20.18 ± 0.05	0.74 ± 0.05	0.50 ± 0.10	0.77 ± 0.09

NOTE.—Cols. (1) MDS field and galaxy ID within field. (2) Number of individual measurements. (3) Mean F785LP magnitude within 5.″2 radius, and dispersion (standard deviation). (4) Mean half-light radius (arcseconds) and dispersion. (5) Mean disk scale length (arcseconds) and dispersion. (6) Measured disk-to-total ratio; the disk contribution was estimated from profile fits (see text); MDSW2-9 was fit by a pure exponential disk in two cases.

5.1. *Direct Comparisons with Other Measurements*

Windhorst et al. (1994) have published deconvolved images and profile fits for six bright galaxies in the MDSW2 field. Five of these galaxies are included in our sample: Windhorst et al. galaxies 2, 3, 4, 5A, and 5B are the same as MDSW2-12, 1, 6, 14, and 13, respectively. A comparison of half-light radii and disk scale lengths shows reasonable agreement, although some significant differences exist. Most of the differences can be attributed to differences in measurement techniques or ranges. For example, in galaxy MDSW2-6, Windhorst et al. fit the disk profile beyond the end of the bar, whereas we fit over the entire disk interior to (as well as beyond) the bar and hence derive a shorter scale length (1.″4 vs. their 2.″3). In addition, Windhorst et al. fit an exponential disk or a $r^{1/4}$-law bulge independently in the regions where the disk or bulge appeared to dominate; we have made simultaneous fits over the usable profile. The independent fits will generally be slightly biased toward too-short disk scale lengths (when a significant bulge is present) and too-large bulge effective radius (when a significant disk is present). These expectations appear to be borne out in the comparison of our measurements.

The six MDSW1 galaxies in our sample were also measured by G94, who fit galaxy models directly to the raw data—a method quite different from ours. Excluding one extended galaxy at the edge of the CCD, the rms deviation between the $r_{1/2}$ measurements is 14%, consistent with $\sim 10\%$ errors in both studies. Relative I_{785} magnitudes agree to ~ 0.12 mag, again consistent with our estimated errors.

5.2. *Double Nuclei and Paired Galaxies*

A detailed analysis of galaxy pairs and possible interaction/mergers in MDS fields will be given elsewhere (e.g., Casertano et al. 1995), but it is useful here to summarize qualitatively the results from our sample. As a working definition we define a "double nucleus" to be a system in which two central concentrations of comparable brightness are separated by less than 10 pixels and embedded within a common envelope. We call two galaxies a "pair" when they are both brighter than our magnitude cutoff ($I_{785} \sim 20.4$) and a "close pair" when there is some indication for a tidal interaction between the two, e.g., distorted outer isophotes. If there are nearby fainter systems, they are generally labeled as "companions." Such systems are noted

PLATE 2

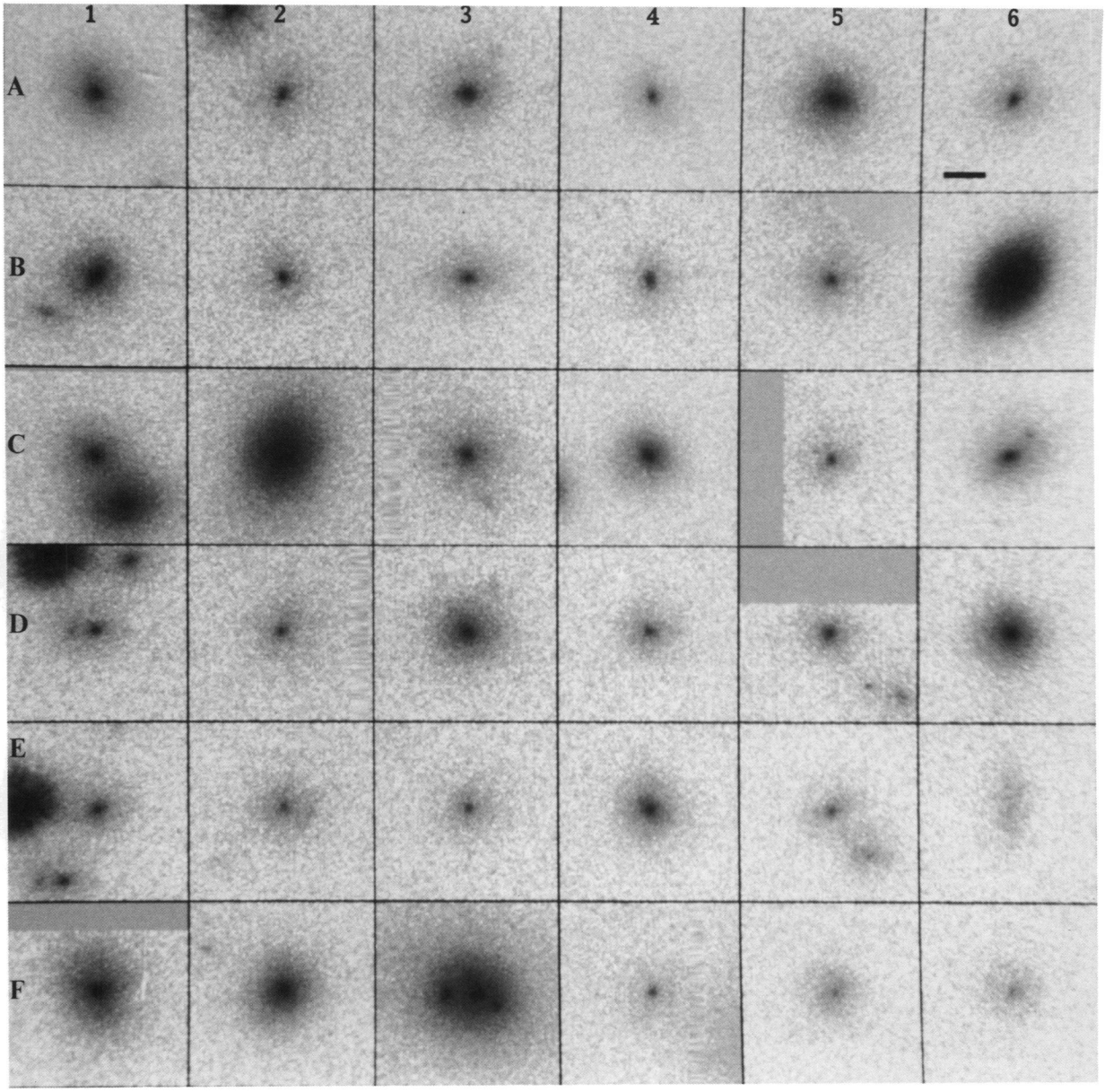

FIG. 9.—Montage of unrestored sample galaxy images, ordered by bulge-dominated through disk-dominated systems. Edge-on and unfittable systems are grouped at the end. (See text for further description.)

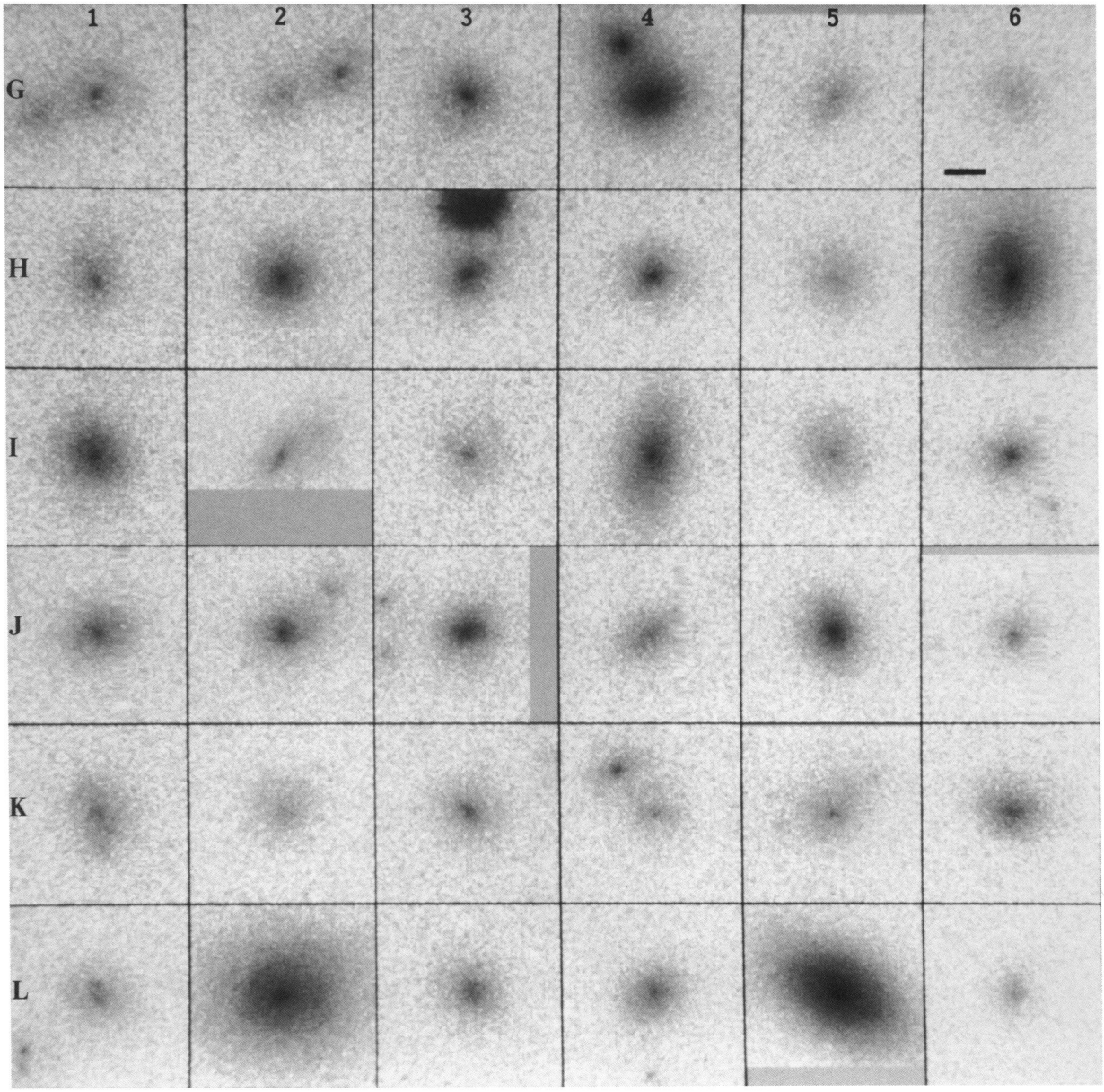

FIG. 9—*Continued*

PLATE 4

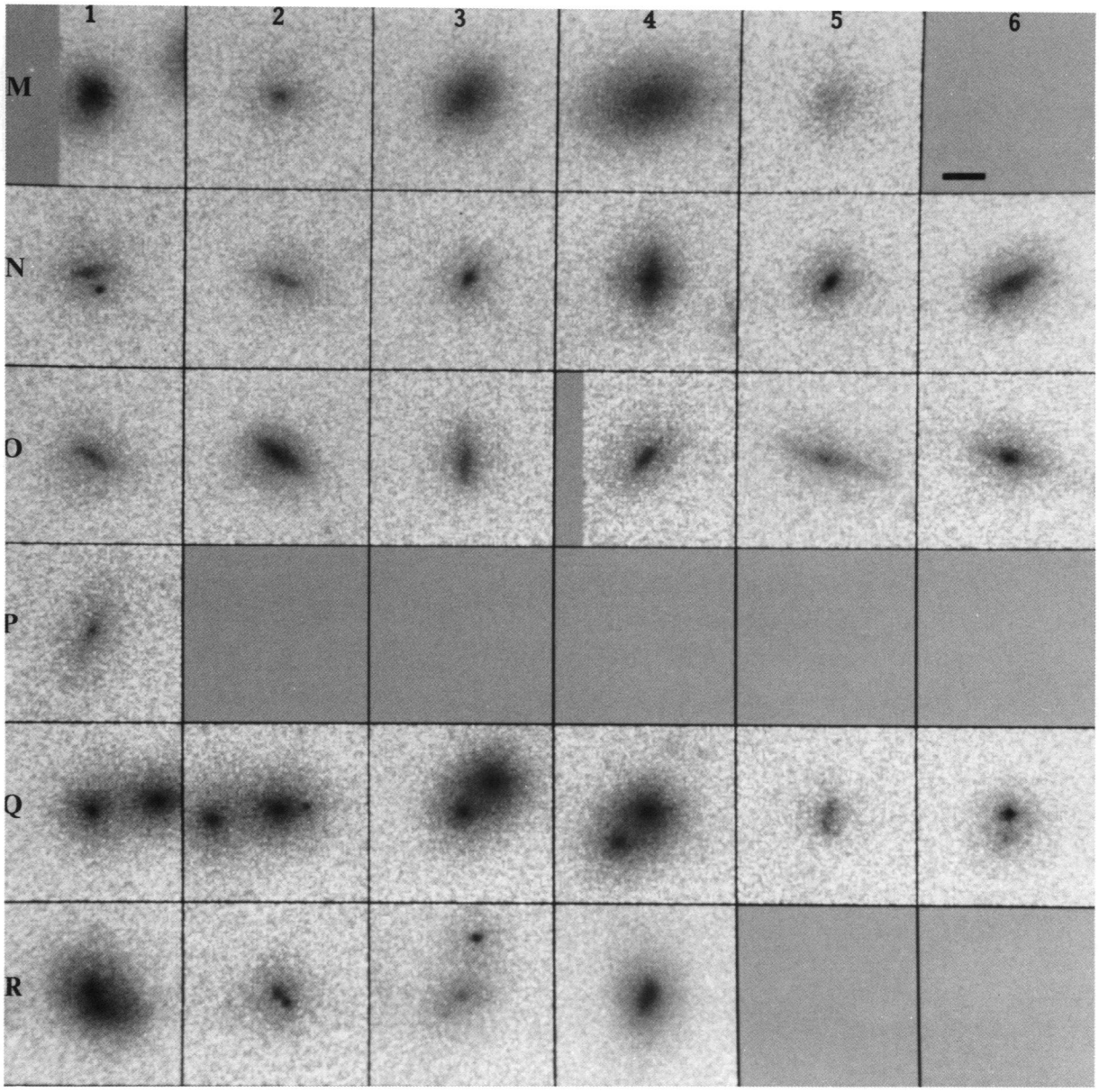

FIG. 9—*Continued*

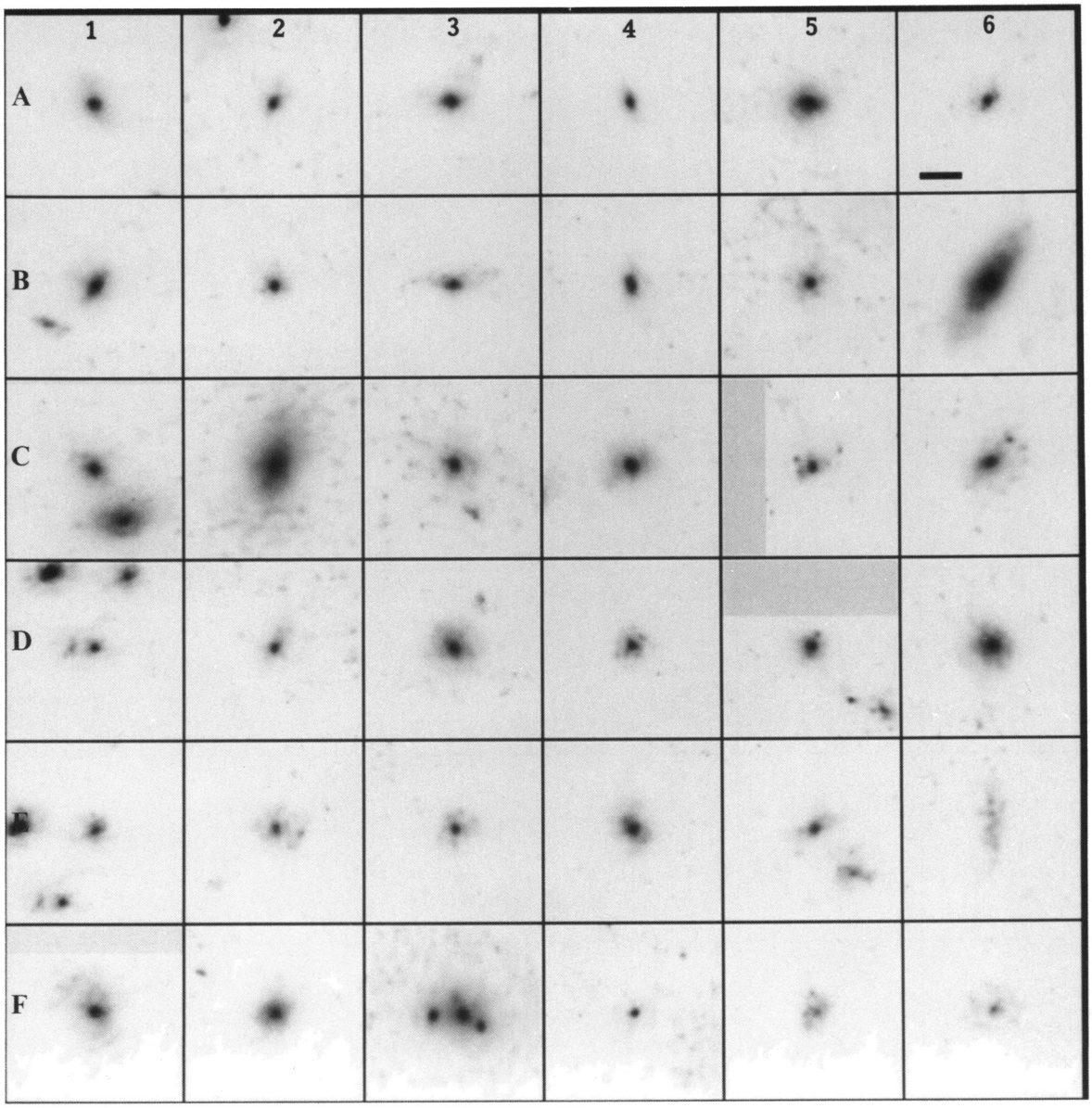

FIG. 10.—Montage of deconvolved images of sample galaxies ordered by bulge-dominated disk-dominated systems

PHILLIPS et al. (see 444, 30)

PLATE 6

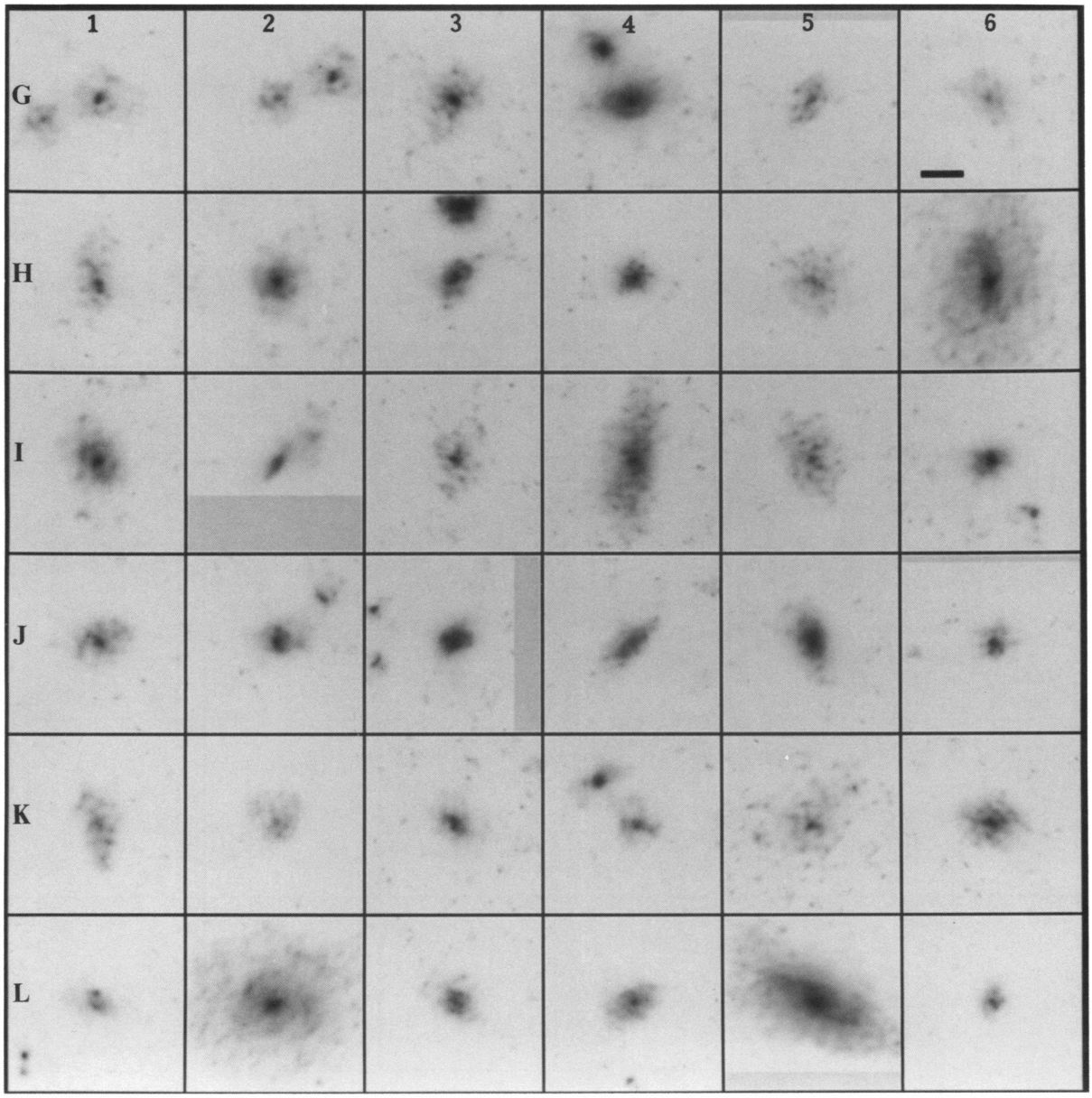

FIG. 10—*Continued*

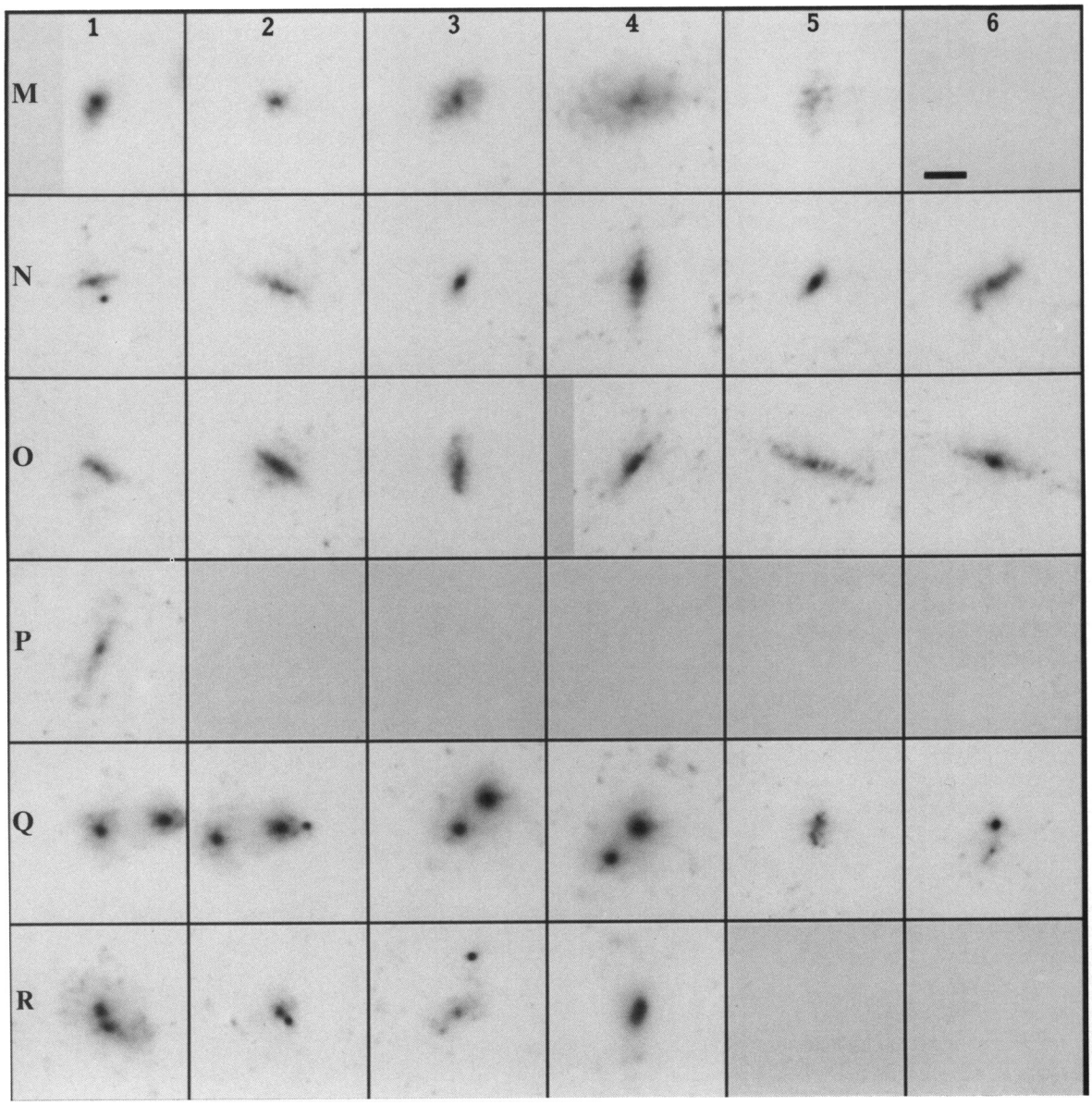

FIG. 10—*Continued*

TABLE 3

MEASURED GALAXY PARAMETERS

MDS-ID (1)	α(2000) (2)	δ(2000) (3)	I_{785} (4)	$\sigma(m_I)$ (5)	$r_{1/2}$ (6)	r_d (7)	$\sigma(r_d)$ (8)	D/T (9)	Atlas (10)	Comments (11)
W1–1	12:29:04.64	+02:10:06.9	19.27	0.03	0.80	...	...	...	R4	dN,tides
W1–2	12:29:04.44	+02:10:24.2	19.57	0.03	0.63	0.54	0.11	0.13	A1	cmp
W1–3	12:29:02.77	+02:09:09.1	19.33	0.03	0.49	0.57	0.12	0.53	C4	pr(1–4)
W1–4	12:29:02.76	+02:09:14.3	19.39	0.03	0.58	0.39	0.00	1.00	M1	pr(1–3),Pne
W1–5	12:29:05.09	+02:08:21.8	20.09	0.03	1.33	0.78[a]	0.12	0.88	I2	late,Pne
W1–6	12:29:02.62	+02:08:06.2	20.50	0.04	0.46	0.32	0.03	0.27	A4	...
W2–1	13:12:21.47	+42:37:23.1	17.74[c]	0.03	1.74[c]	1.23[c]	0.06	0.87[c]	H6	bar,arms
W2–2	13:12:08.51	+42:37:39.2	19.51	0.03	0.82	0.47[a]	0.01	0.95	K6	cmp
W2–3	13:12:13.15	+42:38:35.8	20.18	0.04	0.46	0.53	0.06	0.53	C5	Pne
W2–4	13:12:13.69	+42:39:45.9	20.06	0.04	0.71	0.40[a]	0.01	(0.85)	N1	E(D),stcmp
W2–5	13:12:13.74	+42:39:31.2	20.64	0.06	0.51	0.32	0.01	0.99	L6	...
W2–6	13:12:21.22	+42:39:22.3	17.71[c]	0.03	1.79[c]	1.42[c]	0.09	0.96[c]	L2	...
W2–7	13:12:17.38	+42:39:11.6	19.56[c]	0.03	0.70[c]	0.45[c]	0.03	0.91[c]	J2	clpr
W2–8	13:12:18.60	+42:38:43.6	20.09[c]	0.04	0.77[c]	0.48[a,c]	0.00	0.95[c]	L1	dN?,cmp
W2–9	13:12:19.76	+42:38:32.8	20.18[c]	0.04	0.74[c]	0.50[c]	0.02	(0.77)[c]	N2	E(D)
W2–10	13:12:21.27	+42:38:44.9	20.15	0.05	1.16	1.15	0.10	0.70	E6	Irr(?)
W2–12	13:12:25.08	+42:37:46.5	17.51	0.03	0.65	1.51	0.27	0.44	B6	...
W2–13	13:12:23.85	+42:37:11.9	18.43	0.03	1.04	0.65	0.01	0.82	G4	clpr(2–14)
W2–14	13:12:23.67	+42:37:09.9	18.96	0.03	1.19	0.54	0.04	0.45	C1	clpr(2–13)
W2–15	13:12:26.04	+42:37:19.1	20.11	0.04	1.07	...	...	...	R3	cplx,stcmp
W2–16	13:12:26.05	+42:37:19.1	20.30	0.04	0.33	0.30	0.02	(0.24)	N3	E(B)?
W2–17	13:12:26.35	+42:38:47.2	19.02	0.03	0.72	0.48	0.00	0.92	J5	...
W2–18	13:12:23.41	+42:39:07.3	19.05[c]	0.03	0.96[c]	0.57[c]	0.02	0.86[c]	H2	...
W2–19	13:12:27.59	+42:39:01.5	19.11	0.03	0.48	0.32	0.00	0.29	B1	cmp
W3–1	10:04:22.82	+28:57:48.4	17.70	0.03	1.32	0.88	0.06	0.48	C2	...
W3–2	10:04:19.28	+28:58:05.7	17.67	0.03	1.54	0.68	0.04	0.73	F3	multi-N,cmp
W3–3	10:04:19.21	+28:58:27.1	19.00	0.03	0.68	0.45	0.01	0.73	F2	...
W3–4	10:04:21.80	+28:57:44.2	19.15	0.03	0.67	0.56	0.02	(0.53)	N4	E(D+B)
W3–5	10:04:21.51	+28:58:01.0	19.67	0.03	0.52	0.41	0.02	0.63	E4	...
W3–6	10:04:20.79	+28:58:22.9	19.65	0.03	0.40	0.30	0.03	0.20	A3	...
W3–7	10:04:24.00	+28:58:00.7	19.46	0.03	0.58	0.71	0.04	0.44	B5	Psc
W3–8	10:04:24.48	+28:57:45.1	20.19	0.04	0.42	0.28	0.01	0.59	D5	cmp,Pne
W3–9	10:04:18.90	+28:57:59.9	20.06	0.04	1.38	0.92	0.11	0.74	F4	cmp,Psc
W3–10	10:04:16.76	+28:58:01.7	19.28	0.03	0.64	0.48	0.02	0.57	D3	cmp
W3–11	10:04:15.80	+28:57:33.2	19.89	0.04	1.03	0.85	0.14	0.93	K1	...
W3–12	10:04:18.06	+28:57:07.8	20.04	0.04	0.34	0.31	0.02	(0.31)	N5	E(B+D)?
W3–13	10:04:16.87	+28:58:11.5	19.88	0.04	0.56	...	...	...	R2	dN?
W3–14	10:04:17.52	+28:57:03.5	20.02	0.04	0.43	0.34	0.01	0.29	A6	...
W3–15	10:04:13.75	+28:58:25.0	19.28	0.03	0.89	0.67	0.09	(0.92)	N6	E(D)
W3–16	10:04:14.31	+28:58:42.5	19.92	0.04	0.90	0.53[a]	0.03	(0.77)	O1	E(D)
W3–17	10:04:10.56	+28:58:42.1	20.12	0.04	0.64	0.40	0.02	0.94	K3	cmp
W3–18	10:04:15.99	+28:58:25.9	20.58	0.06	0.51	0.32	0.01	1.05	M2	...
W3–19	10:04:17.81	+28:58:52.5	18.73	0.03	0.56	0.35	0.01	0.29	A5	...
W3–20	10:04:20.87	+28:59:17.9	18.98	0.03	0.97	0.70	0.07	0.88	I1	...
W3–21	10:04:16.38	+28:59:40.7	19.29	0.03	0.53	0.33[a]	0.00	0.92	J3	cmp
W3–22	10:04:17.27	+28:58:37.0	19.37	0.03	0.83	0.32	0.05	0.82	G3	...
W3–23	10:04:18.69	+28:59:11.3	20.05	0.04	1.27	0.58	0.03	0.85	G6	cmp
W5–1	15:02:29.17	+66:10:37.1	19.47	0.03	0.79	0.47	0.03	0.53	C6	stellar knot
W5–2	15:02:29.75	+66:11:01.8	19.67	0.03	1.50	0.75	0.06	0.95	K5	cmp
W5–3	15:02:44.05	+66:11:02.4	19.43	0.03	0.71	0.44	0.04	(0.88)	O2	E(D)
W5–4	15:02:48.19	+66:11:28.8	19.36	0.03	0.85	0.52[a]	0.02	1.06	M3	...
W5–5	15:02:49.05	+66:11:00.2	18.43	0.03	1.51	1.17[a]	0.03	1.06	M4	...
W10–1	2:28:29.58	−10:14:44.9	19.91	0.04	0.96	0.63	0.06	0.78	G1	clpr(10–2)
W10–2	2:28:29.72	−10:14:42.9	20.28	0.04	0.81	0.49	0.02	0.78	G2	clpr(10–1)
W10–3	2:28:29.89	−10:14:27.7	20.32	0.05	0.76	0.50	0.02	0.83	G5	...
W10–4	2:28:33.64	−10:13:21.8	20.01	0.04	1.02	0.78	0.14	0.85	H1	...
W10–5	2:28:34.78	−10:13:37.3	20.49	0.06	0.93	0.55[a]	0.02	1.09	M5	...
W10–6	2:28:36.57	−10:14:07.8	18.58	0.03	0.59	...	...	...	Q4	clpr(10–7)
W10–7	2:28:36.44	−10:14:08.4	18.95	0.03	1.36	...	...	...	Q3	clpr(10–6)
W10–8	2:28:40.67	−10:14:27.8	19.20	0.03	0.55	...	...	...	Q2	clpr(10–9),Psc
W10–9	2:28:40.55	−10:14:30.3	19.36	0.03	0.77	...	...	...	Q1	clpr(10–8),Psc
W10–10	2:28:40.20	−10:14:03.0	19.22	0.03	0.84	0.44	0.04	0.49	C3	cmp
W10–11	2:28:39.51	−10:14:24.6	20.30	0.04	0.62	0.47	0.05	0.66	E5	clpr(10–12)
W10–12	2:28:38.70	−10:14:17.0	20.32	0.04	0.73	0.45	0.01	0.94	K4	clpr(10–11)
W10–13	2:28:39.86	−10:14:08.5	20.09	0.05	0.58	0.59	0.03	0.56	D2	...
W10–14	2:28:35.33	−10:15:18.6	18.73	0.03	0.61	0.42	0.01	0.60	D6	...
W10–15	2:28:37.52	−10:15:55.9	19.67	0.04	0.59	0.42	0.02	0.90	I6	cmp
W11–1	23:04:36.92	+03:07:19.2	20.19	0.05	0.71	0.71	0.07	(0.97)	O3	E(D)
W11–2	23:04:37.81	+03:07:56.4	20.01	0.04	0.76	0.40	0.06	0.61	E2	...
W11–3	23:04:39.18	+03:08:19.4	20.18	0.05	0.35	0.35	0.01	0.34	B2	...
W11–4	23:04:37.69	+03:09:01.8	20.62	0.06	0.72	0.45	0.03	0.76	F6	...
W11–5	23:04:41.38	+03:08:35.5	20.00	0.04	0.38	0.23	0.01	0.39	B4	...
W11–6	23:04:44.22	+03:07:48.6	19.92	0.04	0.75	0.68[a]	0.03	0.92	J4	...
W12–1	22:17:11.13	+00:13:55.5	19.80	0.04	0.72	0.40	0.01	(0.51)	O4	E(D+B),Pne
W12–2	22:17:06.69	+00:14:14.4	20.18	0.05	0.95	0.75	0.07	0.88	I3	...
W12–3	22:17:09.44	+00:13:33.0	19.95	0.04	1.37	0.84	0.14	(0.48)	P1	E(D+B)
W12–4	22:17:16.35	+00:13:49.8	18.54	0.03	0.97	0.80	0.04	0.70	F1	Pne
W12–5	22:17:13.59	+00:13:22.9	19.84	0.04	0.41	0.31	0.02	0.19	A2	Psc
W12–6	22:17:12.53	+00:13:31.9	20.18	0.05	0.58	0.45	0.02	0.62	E3	...
W15–1	20:05:06.22	−55:46:50.0	19.51	0.03	0.68	0.44	0.01	0.86	H3	Psc
W15–2	20:04:59.45	−55:47:11.5	19.73	0.03	0.83	0.56	0.02	0.90	J1	cmp,Pic
W15–3	20:05:02.35	−55:46:36.7	20.06	0.04	0.48	0.40	0.04	0.35	B3	...
W15–4	20:04:59.02	−55:46:46.6	19.93	0.03	1.25	0.61	0.03	0.86	H5	...

TABLE 3—*Continued*

MDS-ID (1)	α(2000) (2)	δ(2000) (3)	I_{785} (4)	$\sigma(m_I)$ (5)	$r_{1/2}$ (6)	r_d (7)	$\sigma(r_d)$ (8)	D/T (9)	Atlas (10)	Comments (11)
W15–5	20:05:00.10	−55:48:09.9	18.62	0.03	1.27	...	...	...	R1	dN,cmp
W15–7	20:04:59.32	−55:48:25.2	19.81	0.03	0.57	0.31[a]	0.00	0.86	H4	stcmp
W15–8	20:04:57.32	−55:48:25.7	20.18	0.04	0.48	0.32	0.02	0.60	E1	cmp,Psc
W15–9	20:04:57.41	−55:47:45.9	19.83	0.03	0.19	...	...	...	Q6	star?
W15–10	20:04:57.29	−55:48:21.9	19.91	0.04	0.83	0.77	0.11	0.56	D1	clpr?,cmp,Psc
W15–11	20:05:00.55	−55:48:32.2	20.18	0.04	0.48	0.33	0.02	0.57	D4	...
W15–12	20:04:54.21	−55:47:51.2	17.41	0.03	1.50	1.30	0.11	0.99	L5	bar(?),arms,Pne
W15–13	20:04:50.97	−55:48:16.9	19.68	0.03	1.28	1.41	0.16	(0.56)	O5	E(D),cmp
W15–14	20:04:47.24	−55:47:11.3	20.30	0.04	0.55	0.32	0.01	0.92	J6	Pic
W15–15	20:04:51.10	−55:47:13.5	20.28	0.04	0.90	0.50[a]	0.06	0.94	K2	...
W15–16	20:04:50.88	−55:46:37.7	19.69	0.03	0.76	0.56	0.06	0.99	L4	cmp
W15–17	20:04:53.38	−55:46:52.8	20.27	0.05	0.64	0.37[a]	0.02	0.75	F5	arms(?)
W16–1	2:17:32.26	+01:42:58.2	19.83	0.04	0.74	0.44	0.02	0.97	L3	...
W16–2	2:17:31.70	+01:43:07.1	19.69	0.04	1.11	0.79	0.11	0.89	I5	...
W16–3	2:17:37.34	+01:43:42.5	19.59	0.03	0.72	0.64	0.09	(0.48)	O6	E(B+D)
W16–4	2:17:38.33	+01:43:17.0	20.58	0.06	0.55	...	...	...	Q5	Irr?
W16–5	2:17:39.22	+01:41:40.3	18.55	0.03	1.41	1.38	0.07	0.89	I4	Pic
W2–11	13:12:22.11	+42:37:54.8	16.99	0.03	0.19	...	...	0.00[b]	...	star
W2–20	13:12:22.90	+42:39:10.3	18.54	0.03	0.21	...	...	0.00[b]	...	star
W15–18	20:04:56.92	−55:48:24.6	17.92	0.03	0.18	...	...	0.00[b]	...	star

NOTE.—Cols. (1) MDS field and galaxy ID within field. (2) and (3) right ascension and declination of galaxy center. (4) and (5) Apparent F785LP magnitude in 5.″2 radius aperture (deconvolved image), and error. (6) Half-light radius of deconvolved image (arcseconds). (7) and (8) Scale length of exponential disk, and error (arcseconds). (9) Disk-to-total ratio: disk estimate from off-axis profile fit, total from photometry (unreliable for edge-on systems). (10) Location of image in the atlas. (11) Comments: pr = pair; clpr = close pair (probable interaction); dN = double nucleus; cplx = complex structure; Irr = irregular; E = edge-on or high inclination; D = disk; B = bulge; N = nucleus; cmp = companion(s); stcmp = stellar (unresolved) companion; P = problems (ne—near edge of CCD; sc—contamination from nearby bright star; ic—interpolated columns within galaxy image).

[a] Exponential fit only.

[b] $r^{1/4}$-law fit only.

[c] Average of multiple measurements.

in column (11) of Table 3. We find several double nucleus galaxies (MDSW1-1, W2-8, W3-13, and W15-5) and even one system (MDSW3-2) in which three (and possibly four) distinct "nuclei" can be identified. In MDSW1-1, tidal features can be clearly seen emanating from the galaxy. Close pairs include one such system in the MDSW2 field (W2-13/14) and four in the MDSW10 field. They include galaxy numbers W10-13/14 (a pair of spiral galaxies), W10-6/7 (two bulge-dominated systems), W10-8/9 (two galaxies with a nearby star), and W10-11/12 (a highly distorted pair). It is somewhat intriguing that four (out of five) close pairs occur in only one field.

A crude estimate of the number of interacting galaxies in our sample can be gained by considering the double nucleus galaxies and close pairs, i.e., systems for which there is possible morphological evidence for a merger or interaction. The total number of such systems in our sample is 10, or 10%.

6. DISCUSSION

6.1. *Galaxy Counts and Sample Completeness*

The effective area of our sample, 0.015 deg^2, is too small to be of value for the study of galaxy counts, but the counts provide a valuable check of our completeness.

I_{785} magnitudes were converted to I using the relation $I \simeq I_{785} + 0.12$. This formula is based on the conversion between the Johnon-Cousins *UBVRI* system and the WFPC system given in Harris et al. (1991) and assumes a characteristic $V-I$ value of 1.4 for our galaxies. This conversion is only mildly color dependent: for galaxy colors $1.0 \leq V-I \leq 1.8$, $I_{785} - I$ ranges only from -0.09 to -0.21.

Figure 11 shows our counts per half-magnitude bins. Also shown are counts from Hall & Mackay (1984), Koo (1986), Tyson (1988), Lilly et al. (1991), and Neuschaefer & Windhorst (1955). The Koo N-band magnitudes have been converted by the relation $I \simeq N - 0.03$ (Majewski 1992) assuming a typical $(R-I)$ color of 1.0 mag; similarly, the Lilly et al. (1991) magnitudes have been converted by their relation, $I \simeq I_{AB} - 0.48$. The Neuschaefer & Windhorst counts have been transformed from the Gunn i band by $I \sim i - 0.78$, using the relation between N and I above and $N \sim i - 0.75$ (Windhorst et al. 1991). We see very good overall agreement between our counts and the other samples for $I \leq 20.5$. A formal maximum-likelihood fit to our data brighter than $I = 20.5$ gives a slope of 0.50, a value consistent with the 0.45 and 0.54 slopes at $18 < I < 20.25$ found by Koo (1986) for two much larger fields, and in excellent agreement with the data of Neuschaefer & Windhorst. Within the variations expected from Poisson fluctuations and the known small-scale clustering of field galaxies, we conclude that our sample is virtually complete at I magnitudes brighter than 20.5, or $I_{785} \lesssim 20.4$.

6.2. *Qualitative Morphology*

The deconvolved images of our sample in Figures 9 and 10 exhibit a wide diversity of galaxy morphology, a finding consistent with distant galaxies observed in both field (G94; Forbes

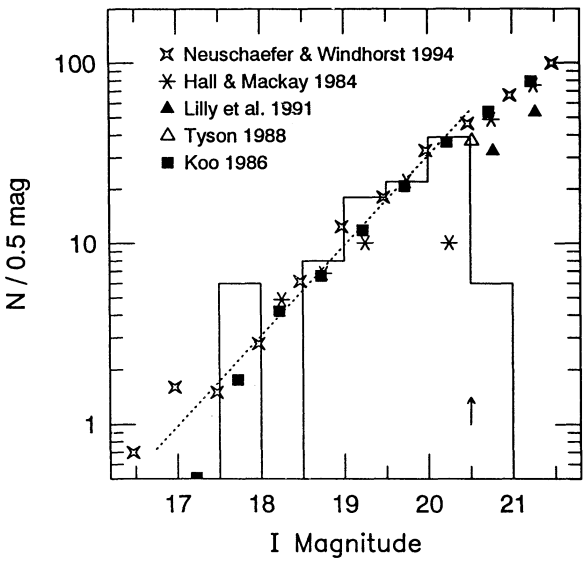

FIG. 11.—Galaxy counts from our sample, which covers 0.015 deg^2. Our I magnitudes have been derived from I_{785} as described in the text. Counts from other works, scaled to our effective area, are shown for comparison. The arrow indicates our completeness limit. The dotted line is a formal linear fit to our counts above the completeness limit, weighted for Poisson statistics.

et al. 1994; Griffiths et al. 1994b) and cluster samples (Dressler et al. 1993). Our sample differs from these other *HST* samples of distant galaxies in being over 2 mag brighter. Assuming a resolution element of ~0".2 and noting the galaxies in Table 3 have a median half-light radius of ~0".7 (within which the S/N is assumed adequate for detecting morphological features), we then expect to have ~40 resolution elements to distinguish more complex structure. Some of the galaxies show elongations that may be bars (W2-1 and W15-2) or inclined disks (W2-4 and W15-13) as well as hints of more complex structure such as spiral arms (W2-1, W15-12, and W15-17). For our sample, a noteworthy pattern is that virtually every galaxy has a bright central component, with the vast majority of galaxies being reasonably bisymmetric. Such relatively simple morphology is characteristic of more luminous galaxies nearby, whether early-type spirals and ellipticals or later-type spirals (Sandage & Bedke 1988). By luminous, we mean galaxies that are close to L^* of the local luminosity function. Given that we expect the typical galaxy in a brighter magnitude-limited sample to be an L^* galaxy (Kron 1980), the morphological characteristics of the galaxies in our sample are not unexpected. In contrast, fainter samples are expected to be increasingly dominated by galaxies with lower luminosities and, due to favorable K-corrections, by bluer galaxies. Such galaxies (e.g., Hubble types Sdm and Im) frequently show strong asymmetries, multiple high-surface brightness components, and lack of central concentration (Sandage & Bedke 1988). These more complicated structures are indeed found to be more common in fainter *HST* galaxy samples, such as those shown in G94 and Dressler et al. (1993), as well as in excellent ground-based images of faint blue galaxies (Lavery et al. 1992; Giraud 1992; Lilly 1993).

6.3. *Disk-to-Total Distributions*

The distribution of disk-to-total ratios in our faint galaxy sample provides another means of evaluating the relationship of galaxies at earlier epochs with contemporary galaxies. In particular, variations in D/T ratios could reflect differences in disk star formation rates, stellar populations, dust content, etc.

Using the technique discussed in § 4.3, we were able to make successful D/T estimates for 77 galaxies; the distribution of the actual measurements is shown in Figure 12*a*. For comparison, we consider the surface brightness analysis of nearby, bright galaxies by Kent (1984, 1985). The Kent sample was selected for a uniform sampling by Hubble type and is known to underrepresent late-type spirals in the field. To correct for this, we compared the fraction of galaxies within each Hubble type in

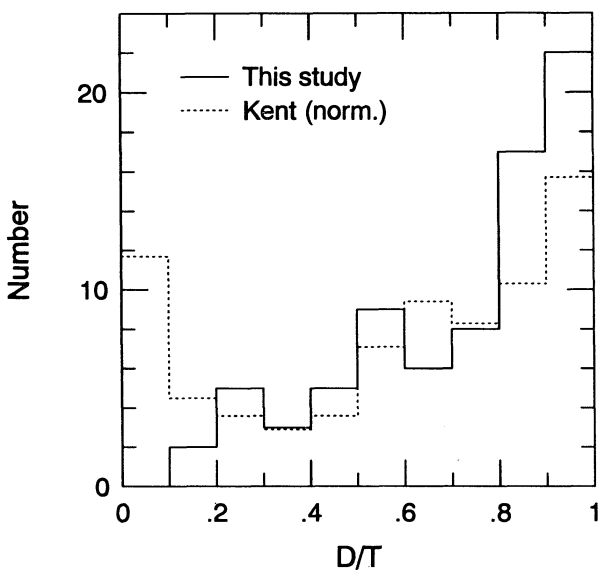

FIG. 12*a*

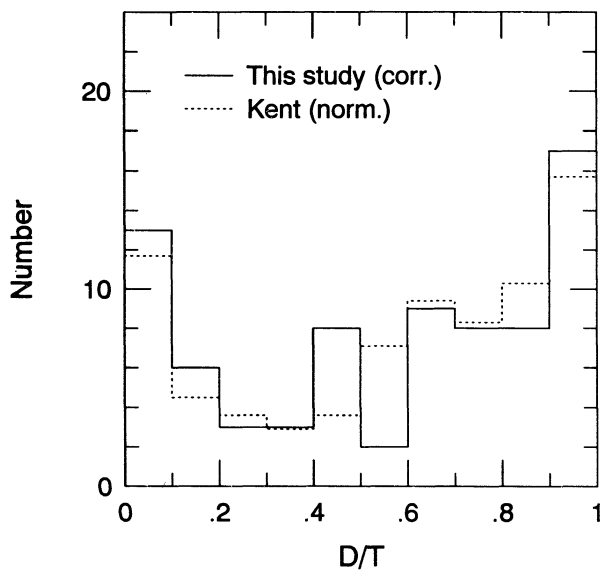

FIG. 12*b*

FIG. 12.—(*a*) Distribution of actual D/T measurements for our sample galaxies. Edge-on galaxies have been excluded. The "normalized" Kent sample is shown for comparison (see text). (*b*) Distribution of D/T measurements after the empirical correction has been applied to remove systematic biases. We see that after correcting (statistically) for sytematic biases, there is good agreement between our sample and the normalized Kent sample.

the Kent sample with the corresponding fraction in the Revised Shapley-Ames Catalog (RSA; Sandage & Tammann 1981). We then scaled the D/T distribution found by Kent within each Hubble type to match the RSA distribution of types and scaled these numbers to give a total of 77 galaxies. We refer to this as the "normalized" Kent sample, and it is also shown in the figure.

We know from § 4.3 that there are systematic biases in our measurements of D/T, but they are small above ~ 0.7. From this, we might conclude that there are somewhat more disk-dominated galaxies in our sample than in the normalized Kent sample. However, when we apply the empirical correction for the systematic errors (§ 4.3), we find the distribution shown in Figure 12*b*. This distribution shows a remarkable similarity to the normalized Kent sample. The corrections are so large that this striking similarity is almost certainly fortuitous, but this figure demonstrates that there is no compelling evidence that the distribution of morphological types in our sample differs strongly from that of nearby galaxies.

The corrections applied to the D/T measurements are large and model dependent. An alternative measurement that is not so strongly dependent on corrections is the ratio of disk scale lengths (r_d) to the overall half-light radius of the galaxy ($r_{1/2}$). This ratio depends on the size of the bulge with respect to the disk as well as the bulge-to-disk ratio and is another distance-independent quantity. In Figure 13, we show the distribution of these ratios compared to the normalized Kent sample. Both samples show a peak slightly above the ratio expected for a pure exponential disk, shown by an arrow in the figure. There is overall good agreement between the two samples, although the peak of our distribution appears shifted toward larger r_d or smaller $r_{1/2}$. A small shift in this sense is expected since our $r_{1/2}$ is measured in a circular aperture whereas Kent's are corrected to face-on orientation; for inclined galaxies, our $r_{1/2}$ measures will thus be slightly smaller than they would be in Kent's sample. Again, we find evidence that the range in galaxy structure is similar in our sample and in the normalized Kent sample.

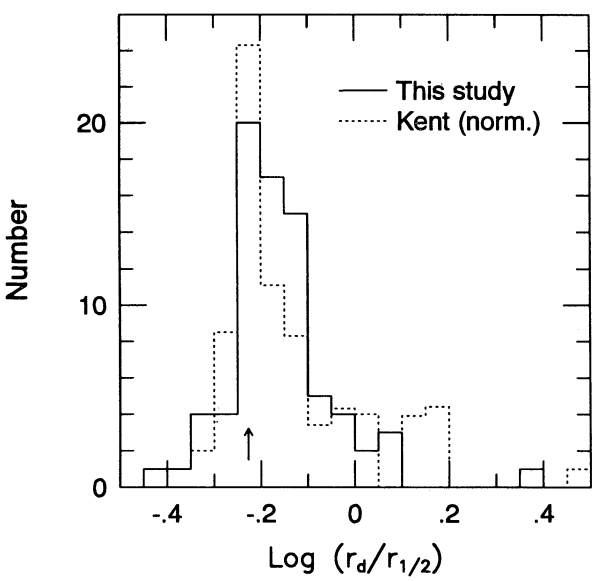

FIG. 13.—Distribution of the distance-independent ratio of disk scale length (r_d) and overall half-light radius ($r_{1/2}$), both for our sample and the "normalized" Kent sample. The arrow marks the expected ratio for a pure (nontruncated) exponential disk viewed face-on.

We have not yet considered whether we *expect* the galaxies in our sample to have D/T and size-ratio distributions consistent with those of the normalized Kent sample. In fainter magnitude-limited samples, galaxies of lower luminosity and bluer color should increase in relative number. On the other hand, the RSA is magnitude selected in a bluer passband than that of our observations. To some degree, these two biases should offset each other, and to the extent that they do, we may say that we see little evidence in our sample for bulge-to-disk evolution. However, to quantify precisely how the two effects (fainter magnitude limit and redder passband) interact requires detailed knowledge of the multivariate distribution of galaxy D/T, luminosity, and color. Such information is not available for any statistically complete sample of galaxies.

6.4. *Angular Size versus Magnitude*

The apparent size-magnitude distribution of galaxies is a powerful tool for exploring galaxy evolution. Here we examine whether evolution in size and luminosity has occurred in the galaxy population at the intermediate redshifts probed by our sample. Even without direct redshift information, the size-magnitude distribution provides constraints on galaxy evolution because rest-frame size and luminosity for local galaxies are strongly correlated. The apparent size and magnitude distribution of galaxies based on a nonevolving model can therefore be predicted reliably and compared to the observed distribution.

While we have a variety of choices for characterizing the size of galaxies, we selected the half-light radius ($r_{1/2}$) because of its robustness to uncertainties in the deconvolution process; i.e., any systematic errors in measurements of $r_{1/2}$ are small and are only weakly dependent on morphology. Moreover, $r_{1/2}$ is independent of isophote thresholds and is a metric radius, by which we mean that two identical galaxies observed at different distances will have half-light radii in inverse proportion to their angular-size distances.

For the size-magnitude comparison, we have again chosen Kent's (1985) sample as a fiducial. Although Kent describes the selection of his sample to be biased toward luminous galaxies, the absolute magnitude distribution of his sample is symmetric with a peak within 0.5 mag of M^* and with FWHM of 1.5 mag. This is roughly what one would find in a complete magnitude-limited sample at bright magnitudes, except that such a sample would have a luminosity distribution about twice as wide (cf. Fig. 1 of Schechter 1976). The fact that Kent's sample underrepresents low-luminosity systems is not a problem for our comparison, as will become apparent below. The advantage of Kent's study for our purposes is that he has measured half-light radii and total magnitudes for these objects in the Gunn r band. At the expected characteristic redshift of our survey ($z \simeq 0.3$; see below), this bandpass corresponds quite closely to our observed F785LP band ($1.3\bar{\lambda}_r = 0.87$ μm compared to $\bar{\lambda}_{785LP} = 0.89$ μm). Kent has also decomposed many of these galaxies into disk and bulge components, and so D/T measurements are available for his sample.

Our data and Kent's are shown in Figure 14*a*, where the apparent half-light radius is plotted against apparent magnitude. The G94 data for objects identified as galaxies are also shown, in order to give some indication of trends at fainter magnitudes. Figure 14*b* shows the region around our sample in more detail. Our bright *HST* sample is an excellent com-

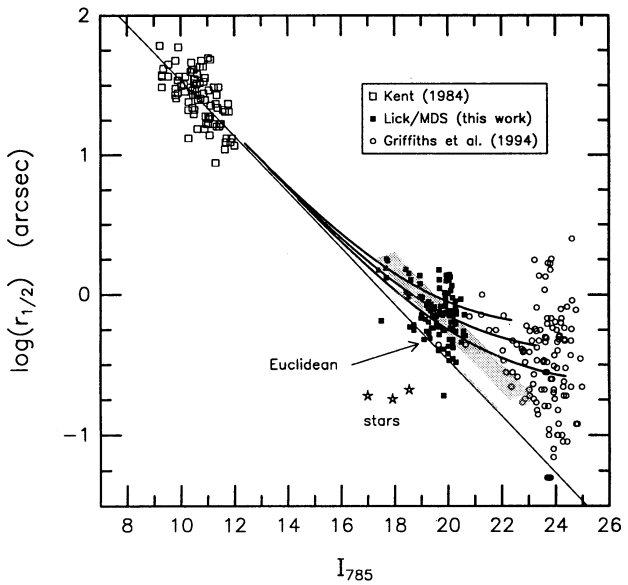

FIG. 14*a*

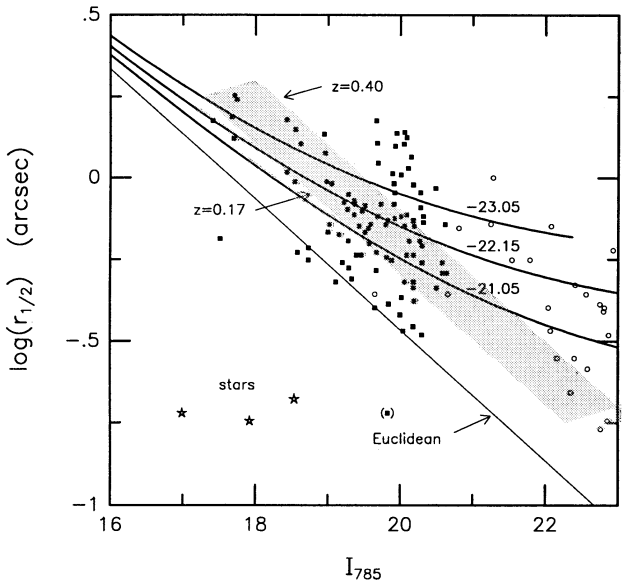

FIG. 14*b*

FIG. 14.—(*a*) Half-light radii of galaxies vs. I_{785} magnitude, for all sample galaxies (*solid squares*). For comparison, we show the sample of Kent (1985), adjusted to I_{785} as described in the text (*open squares*), and the G94 faint galaxy sample from the 3C 273 (MDSW1) field (*open circles*). Stellated symbols represent three known stars in our sample. One sample galaxy, W15-9, has an $r_{1/2}$ similar to the stars; its deconvolved image shows that it is probably a star superimposed on a faint galaxy, with most of the flux coming from the star. Heavy solid lines represent redshift tracks for galaxies of absolute magnitude corresponding to the median and upper and lower quartile luminosities observed in a model nonevolving sample to $I_{785} < 20.5$, described in the text. Rest-frame $r_{1/2}$ are associated with these luminosities using the correlation observed in Kent's sample between total magnitude and $r_{1/2}$ (see text for further details). The tracks are for the absolute magnitudes shown, and $r_{1/2}$ of 6.8 kpc (*upper*), 4.5 kpc (*middle*), and 2.7 kpc (*lower*), assuming $H_0 = 50$, $q_0 = 0.05$, and $\Lambda_0 = 0$. The thin solid line corresponds to galaxies in a Euclidean universe. The shaded area corresponds to the upper and lower quartiles in redshift for the nonevolving model distribution to $I_{785} < 20.5$. (*b*) Enlargement of area round our sample.

plement to the measures made in G94: whereas G94 had virtually no galaxies brighter than $I_{785} \sim 21$ mag, our entire sample falls into this magnitude range and thus roughly doubles the leverage to explore the relationship of size versus magnitude among faint galaxies. Our magnitude range is also particularly valuable as it is where faint galaxy size begins to deviate significantly from the Euclidean line.

In order to compare galaxy sizes as a function of apparent I_{785} magnitude, we exploit the known correlation between rest-frame size and absolute magnitude for all galaxies, e.g., the Second Reference Catalogue (RC2) of de Vaucouleurs, de Vaucouleurs, & Corwin (1976) or Huchra (1977). However, one of the difficulties of using the RC2 or Huchra's Markarian sample data for comparison with galaxies at cosmological redshifts is that sizes are based on an isophotal level. We have therefore used Kent's sample to define the correlation between $r_{1/2}$ and absolute magnitude in the Gunn r band. Adopting $H_0 = 50$ km s^{-1} Mpc^{-1}, this correlation is given by

$$-5 \log r_{1/2} = M(r) + 17.9 ,$$

where $M(r)$ is the absolute magnitude in the Gunn r band and $r_{1/2}$ is in units of kiloparsecs. This relationship assumes constant mean surface brightness within $r_{1/2}$; in reality, there is considerable scatter. We then use a characteristic galaxy color to determine a mean transformation between Gunn r and I_{785} for galaxies at $z \sim 0$, given by $r - I_{785} = 1.0$ mag. To predict the apparent size and magnitude of galaxies as a function of redshift, we adopt a K-correction for a power-law spectral energy distribution of $f_\nu \propto \nu^{-2}$. Such an energy distribution is a reasonable approximation for galaxies observed in the I_{785} band to $z \leq 1$ (Bershady 1995).[5]

In Figure 14, our galaxies display a clear trend to smaller size at fainter magnitudes, consistent with the simple expectation that fainter galaxies are more distant (on the average) and thus appear smaller. In a Euclidean universe where galaxies all have the same mean surface brightness, galaxies would lie along a straight line with a slope of -5. This is represented by the thin solid line, with the zero point defined by Kent's sample. Our sample galaxies and those in the fainter G94 sample lie on (within the scatter expected from the Kent sample) or to the upper right of this straight line, consistent with simple cosmological expectations.

The thick solid curves in Figure 14 represent redshift tracks for model galaxies of three luminosities and sizes for a Friedmann universe with $q_0 = 0.05$ and $\Lambda_0 = 0$. These tracks all have the same average surface brightness interior to $r_{1/2}$. We have truncated these curves when the model redshifts reach $z = 1$, where our adopted K-corrections start to become significantly uncertain. At the expected characteristic redshifts of our sample ($z \sim 0.3$; see below), the difference between $q_0 = 0.05$ and 0.5 geometries is small, so for our current purposes this choice is not important. The luminosities were chosen to represent the median and upper and lower quartiles expected for a nonevolving galaxy population observed to $I_{785} < 20.5$

[5] Near the I band, the observed range in the effective spectral index α (where $f_\nu \propto \nu^\alpha$) is such that there is only a ± 0.15 mag differential in the K-corrections for all galaxies at $z = 0.3$, assuming the value we have adopted, i.e., $\alpha = -2$.

mag. This nonevolving model is based on a fit to observed counts, colors, and redshifts of galaxies from 15th to 25th mag and is similar to that developed by Koo, Gronwall, & Bruzual (1993). The corresponding absolute magnitudes are $M(I_{785}) = -22.15$ (median) and -21.05 and -23.05 mag (quartiles.), where L^* corresponds roughly to $M(I_{785}) = -22.8$ mag. Rest-frames sizes were then chosen to match the luminosities as discussed above. For a nonevolving galaxy population observed to $I_{785} < 23.5$ mag, which corresponds to the depth of the G94 sample, the median and quartile luminosities would shift by ~ 1 mag (fainter). This shift is a reflection of (1) the shape of the luminosity function, (2) the fact that objects appear increasingly fainter with distance in a non-Euclidean universe, and (3) the correlation between color and absolute magnitude such that objects become intrinsically bluer at lower luminosities and are therefore relatively more visible due to favorable K-corrections.

More luminous model galaxies in a Friedmann universe lie farther off the Euclidean curve at a given apparent magnitude because they are at higher redshift, where the effects of geometric curvature on angular size are larger. The effects of curvature on a set of galaxies spanning a range in luminosity and size will therefore produce a trumpet-like broadening of the apparent size-magnitude distribution with increasing magnitude. Galaxies in both our sample and G94 qualitatively follow these non-Euclidean trends. In addition, the G94 sample appears to contain more lower luminosity galaxies, as expected from the reasoning above.

To make a more quantitative assessment of whether our sample is consistent with a nonevolving galaxy population, we have shaded the area spanning the upper and lower quartiles in redshift for the nonevolving model discussed above. For $I_{785} < 20.5$, these quartile redshifts are 0.17 and 0.40, and the median redshift is 0.28. If our data is consistent with the nonevolving model, galaxies in our sample should be centered on this area as well as the region between the quartile magnitude lines in Figure 14.

In the expanded plot, Figure 14*b*, one can count the number of objects in our sample bounded by the quartile luminosity tracks (*solid lines*), as well as the quartile redshift lines (*shaded region*). We find that there are 23 galaxies above and 32 below the area bounded by the solid curves. (We exclude W15-9 from these counts, as noted above.) These numbers are very close to the expected $\frac{1}{4}$ of our sample, namely, 25. The slight excess of counts below the lower quartile line indicates that our sample may be of *slightly* higher intrinsic surface brightness than expected from the nonevolving model. Models including mild evolution show luminosities brighter by (typically) ~ 0.1 mag at $z = 0.15$ and ~ 0.2 mag at $z = 0.4$ (Gronwall 1994). Assuming no change in $r_{1/2}$, these small increases in luminosity would shift the tracks to slightly higher magnitudes, and the upper and lower counts in our sample would be virtually identical.

Recent redshift surveys of comparably faint galaxies (Broadhurst, Ellis, & Shanks 1988; Colless et al. 1990, 1993; Lilly et al. 1991; Lilly 1993) have all shown that the redshift distribution is similar to "no-evolution" predictions for intrinsically luminous galaxies. The size-magnitude data presented here supports this finding. Furthermore, we are given the opportunity to provide an additional check on the models. In Figure 14 we may count the objects falling outside the shaded region, which is bounded by the upper and lower quartile redshifts expected for our magnitude limit, provided our model—and calibration to local galaxies through the Kent sample—is valid. We find 25 galaxies to the right and 28 to the left of the shaded region (again, with 25 predicted for both). Thus, the expected z-distribution from our size-magnitude data is completely consistent with direct redshift surveys.

As a direct check of the redshift distribution predicted by our model, we can compare our quartile redshifts (0.17, 0.28, and 0.40) with the observed distribution to $I_{785} < 20.5$ mag from Lilly (1993) as determined from spectroscopic redshifts. Using the transformation of $I_{785} = I_{AB} - 0.6$, where I_{AB} is in Lilly's magnitude system, galaxies in Lilly's survey to $I_{785} < 20.5$ mag have lower quartile, median, and upper quartile redshifts of 0.21, 0.29, and 0.42, respectively, using Lilly's 3″ aperture magnitudes (sample of nine galaxies), or 0.23, 0.38, and 0.42, respectively, using the isophotal magnitudes (13 galaxies).

Although we have not considered the effects of measurement errors and the intrinsic dispersion due to real galaxies having a finite range of surface brightness, on the whole the observed size-magnitude distribution of our sample is remarkably consistent with what is expected for a nonevolving galaxy population. *We conclude that there is little evidence for significant evolution in size or luminosity for field galaxies with typical redshift of* $0.2 \lesssim z \lesssim 0.4$ *and with luminosities* $M \lesssim M^* + 2$ *mag.*

A final feature in Figure 14 to note is that the smallest galaxies at a given apparent magnitude lie along the track expected for a Euclidean universe. Low-luminosity galaxies at very small redshift should follow this limit.

7. CONCLUSIONS

In summary, we have selected and analyzed a complete sample of 100 galaxies brighter than $I_{785} = 20.4$ from nine *HST* WFC images from the MDS Key Project. This sample of faint galaxies (equivalent to galaxies brighter than $B \sim 22$–23) roughly doubles the magnitude range of the first set of fainter galaxies analyzed by the MDS team (G94; Windhorst et al. 1994). Besides a series of postpipeline processing steps, the galaxy images have been deconvolved to allow visual classification of morphology as well as quantifiable measures of structure. Photometry (total magnitudes) and measures of galaxy profiles (half-light radii, disk scale lengths, and disk-to-total ratios) have been tabulated for our sample.

Our primary finding is that the apparent size and magnitude distribution of our sample of galaxies is roughly consistent with a nonevolving galaxy population observed at a median redshift of $z \sim 0.3$ *for which size and luminosity are correlated as observed in local samples.* This median redshift agrees with the observed spectroscopic redshift distribution of Lilly (1993). Our result implies that there is no evidence for substantial size and luminosity evolution of galaxies brighter than about one-tenth of L^* ($M^* + 2.5$) to redshifts of ~ 0.4.

The distribution of measured disk-to-total ratios (D/T) in these faint galaxies is consistent with local galaxy samples, and the central concentrations and symmetries of our deconvolved galaxy images also compare well with luminous ellipticals and spirals nearby. No exotic processes such as extensive merging, disappearing dwarfs, or a nonzero cosmological constant are needed to explain the apparent distributions of our galaxy sample.

Future work will concentrate on increasing our sample to improve the statistics, adding color information (where available), and developing more realistic models to analyze our data. Many of the difficulties encountered in this work, due to

biases and uncertainty introduced by the deconvolution process, will be avoided with WFPC-II images now becoming available. These images will also allow reliable morphological analysis to much fainter magnitudes (see, e.g., Forbes et al. 1994; Griffiths et al. 1994b). Spectroscopic redshifts will refine the size and surface brightness tests and enable a number of other correlations with size to be explored, e.g., with color, intrinsic luminosity, profile shape, and inclination. Analysis and interpretation of these data also could be facilitated by obtaining more reliable measures of structure in statistically representative samples of nearby galaxies.

We wish to thank other members of the MDS team for helpful comments on the manuscript and for help with the MDS database. We are very grateful to Caryl Gronwall for providing the nonevolving galaxy models, and for valuable discussion. We also thank Carl Grillmair for informative discussions about the WFPC, and Elizabeth Barker for help in understanding WFC PSF characteristics and collating the Kent sample. Support for this work was provided by NASA through grants GO-2684.05-87A and GO-2684.04-87A from the Space Telescope Science Institute, which is operated by AURA, Inc., under NASA contract NAS 5-26555. M. A. B. acknowledges support from NASA through grant HF-1028.01-92A, from the Space Telescope Science Institute, which is operated by the Association of Universities for Research in Astronomy, Inc., under contract NAS 5-26555. D. C. K. acknowledges support by an NSF-PYI grant AST 88-58203.

APPENDIX

IMAGE RECONSTRUCTION

In principle, any astronomical image that has been degraded by a PSF can be reconstructed to the extent permitted by sampling (and noise), provided the PSF is known precisely. In practice, the PSF is never known exactly, and the reconstruction is limited by the confusion between real signal (which has been convolved with the PSF) and noise (which is an additive component introduced after the degradation). We may express this

$$i_j = (a * o)_j + n_j ,$$

where i is the image, o is the true image, a is the PSF, and the subscript j refers to the pixel location. Provided that a is well known and that n_j is negligible we can generally obtain good results with image restoration techniques. However, if n_j is large with respect to the degraded signal, we generally obtain poor restoration. In the MDS images of faint galaxies, the S/N *per pixel* is generally quite low (less than 3) over most of the aberrated image, so noise is a serious problem.

The "noise field," n_j, is typically characterized by photon noise [which depends on the intensity of the "real signal," $(a * o)_j$, including the sky background] and read-out noise. In real data, there are always additional sources of noise, such as noise in the calibration frames. In WFPC images, for example, there are additional components from poorly removed and low-energy cosmic-ray events in the data frames and residual "odd/even" patterns in some calibration frames. However, there are two properties of the noise which we can utilize to help distinguish between noise and real signal. The first is that real signal *cannot be negative*, so that any intensity values below the background level must be due to negative noise fluctuations. This property of the noise has been used in various algorithms (e.g., Lucy-Richardson) to suppress the growth of noise via enforcement of positivity (i.e., negative values are set to zero and thereafter cannot change). The second property is that the noise is uncorrelated, specifically it has not been convolved with the PSF. This means that an isolated noise spike will not be surrounded by broad wings as would be the case for a real object imaged by the WFC.

We have employed these last two properties, along with the assumption that the noise field has an *integrated flux identically equal to zero*, to form an estimate of the noise field, using the method described below. The method is relatively crude, but has the advantage that it is independent of any particular noise model except for the zero-flux assumption. Simulations show that the removal of this estimated noise field permits us to reliably measure galaxy structural parameters to ~ 1 mag fainter than is possible from deconvolutions of the unmodified images.

A.1. METHOD

After subtraction of the sky, the resulting image contains many negative pixels. These values must be set to zero before deconvolution. The difference between the integrated flux of the original image and the zero-truncated image represents an estimate of the power in the noise and also represents an amount of artificial flux we are introducing into the image prior to reconstruction. We take the nonnegative image through a large number of iterations (120) using the Lucy-Richardson algorithm.[6] With positivity enforced, positive noise spikes grow quickly but then "stall" as the flux around them is depleted. The resulting image has much of its flux contained in individual noise spikes, but when we reconvolve with the PSF *the noise is heavily smoothed, while the original degraded image structure is largely recovered.*

This reconvolved image is then subtracted from the original, sky-subtracted image. This difference contains a first estimate of the noise field, as well as the "artificial flux" added by the clipping of negative pixels, and usually also contains obvious residual correlated structure. The source of this residual structure is easy to understand. The process of reconstruction involved redistributing flux into its proper location in the restored image. However, noise spikes will be misinterpreted as the cores of real object images, and so flux is placed in them resulting in too little flux moved into the real objects. As a consequence, the real objects

[6] The actual software used is the ACOADD software of Hook & Lucy (1992), in its single-image mode; this was used in place of the STSDAS LUCY task for historical reasons, but it is equivalent to the latter task with the noise parameters turned off. This is desirable so that the deconvolution is linear, i.e., all parts of the image are restored at the same rate. The STSDAS LUCY task with noise parameters set has the property of slower convergence in lower S/N regions.

are not properly restored, and after reconvolution they tend to be even more degraded than in the original. As a result, the real signal is incorrectly subtracted and the residuals show (generally low-frequency) correlated structure. To remove both the artificial flux and the low-frequency correlated structure, we apply a high-pass filter (in practice, we subtract a Gaussian-smoothed version of the same noise image). This leaves a reasonable estimate of the high-frequency noise (as determined from simulated data) and is the first estimated noise field.

This noise estimate is subtracted from the original image, and the whole deconvolution-reconvolution process is applied again. At each iteration, we relax the effect of the high-pass filter. After three such iterations, we find that the noise has been reduced by about one order of magnitude and shows no apparent correlated structure. A histogram of the estimated noise-field resembles a Gaussian profile with FWHM consistent with the expected photon and read noise properties.

One drawback to this method is that the strongest noise spikes will remain at some level, and they assume a "real" appearance in the restored images; i.e., they become somewhat "resolved" rather than being limited to a single pixel. This is particularly likely to happen on the wings of galaxies. Once again, the reason is easy to understand. The method of noise estimation basically selects features whose flux distribution is inconsistent with a real signal. However, where there is some extended background, as in the wings of images, the algorithm cannot distinguish between a noise spike on a smooth background and a real point source within a hole in an otherwise smooth background. Therefore, we must use caution in interpreting small-scale structures, but for large-scale parameters (such as scale lengths) azimuthal averages should remove the effects of such artifacts.

The final restored image is produced using 25 (nonaccelerated) ACOADD iterations. While this number is relatively small, simulations indicate that it does a good job at restoring extended structure while keeping the remaining noise spikes from growing too much. The disadvantage to such a small number of iterations is that the inner 1–2 pixels in sharply peaked objects are not restored well. For the purposes of measuring the galaxies in this sample, this means that disk scale lengths are quite robust, but bulge effective radii are unreliable for small r_e, especially where the bulge-to-disk ratio is small.

An example of an original image, estimated noise field, and final deconvolved image is shown in Figure 15 (Plate 8).

A.2. TESTS WITH SIMULATED MODEL GALAXIES

For the purposes of testing various deconvolution options and developing the noise-reduction algorithm, we created a set of 84 galaxy models of varying bulge-to-disk values, inclinations, and length scales, using tasks in the IRAF ARTDATA package. The measured disk scale lengths ($r - d$) of the model galaxies are 1.56, 2.61, 4.16, and 6.43 pixels. Bulge-to-disk ratio varies from pure $r^{1/4}$-law bulge to pure exponential disk; the intermediate cases are a superposition of the two with D/T ratios of 0.18, 0.43, 0.62, and 0.85. Four different inclinations were created by setting the axial ratio of the disk (only) at b/a values of 1.0, 0.7, 0.4, and 0.1. We refer to these models as the "original model" images.

We convolved each model with a representative WFC PSF created by TINYTIM Version 2.1 (Krist 1992), scaled in intensity to four different levels separated by 1 mag each, and added a constant background level of 30 counts; this level is somewhat on the high side (but still within the normal range) of what we observe in actual WFC MDS images. The degraded model images then had appropriate photon and readout noise added (based on $7.6e^-$ DN^{-1} and $14e^-$ readout noise.) For comparison with the MDS sample data, the S/N ratios of these model galaxies correspond to $I_{785} \simeq 19.3$–22.3 mag in an averaged set of four 2000 s exposures and ideal noise properties. Real data appears somewhat noisier, and the magnitude range corresponding to these S/N would be slightly brighter. For a single 2000 s exposure and typical observed noise, the models simulate galaxies in the range $I_{785} \sim 18.6$–21.6 mag.

We then deconvolved the models using the standard Lucy-Richardson algorithm, as well as the "noise-reduced" procedure outlined above. In the tests of the standard algorithm, we used the "acceleration" option of the ACOADD software; 16 accelerated iterations is roughly comparable to the 25 nonaccelerated iterations used with the "noise-reduced" procedure applied here and to the actual WFC images. Since we are primarily interested in disk scale lengths and since the inner (bulge) regions of the galaxy images are poorly restored, for the tests below we used the STSDAS tasks ELLIPSE and NFIT1D to measure exponential profile fits to the images. These fits were made over 2.5–8, 3–9, 3.5–10.5, and 4–12 pixels radii for the four disk sizes, respectively. The ranges provide roughly seven points to fit (solving for only two independent variables, the scale length and the central intensity) and cover the region exterior to the central pixels but where there is still significant signal. We can compare the measurements of the reconstructed images with those of the original model images, thereby assuring that any bias introduced by the measurement process is the same in both cases and providing a test of the reconstruction process alone. Note that we are fitting *only* an exponential to the profile—this does not have any "physical" meaning for the elliptical or bulge-dominated models, but we can still compare the fits over the same radii and expect the same results provided the deconvolution has been successful.

First, we explore deconvolutions with the standard Lucy-Richardson algorithm, without noise reduction. Figure 16 shows the effect of decreasing brightness on the scale length measurements. Going to fainter magnitudes, i.e., lower S/N, we start to see systematic deviations from the measurements of the original model scale lengths. In particular, at very low surface brightness the disks are not restored by the deconvolution, and so the measured scale lengths are too large, as shown by the disk-dominated cases of larger angular size. However, those galaxies with moderate or large D/T ratios show a strong tendency toward *too-small* scale lengths at fainter magnitudes. These effects are noticeable in Figure 16*c* and become severe in the lowest S/N case. Figure 17 demonstrates that increasing the number of deconvolution iterations *accentuates* these effects. This is primarily a result of pushing the deconvolution further than warranted by the S/N of the galaxy image and thus "overresolving" the noise.

Finally, in Figure 18 we examine the results of deconvolution following the noise reduction procedure outline above. While the scatter is still large, it is clear that the noise-reduced data have considerably less *systematic* bias than the straight deconvolution without noise reduction, particularly in the larger angular size (i.e., lower surface brightness) models. This demonstrates the real gains to be made by the noise-reduction technique.

PLATE 8

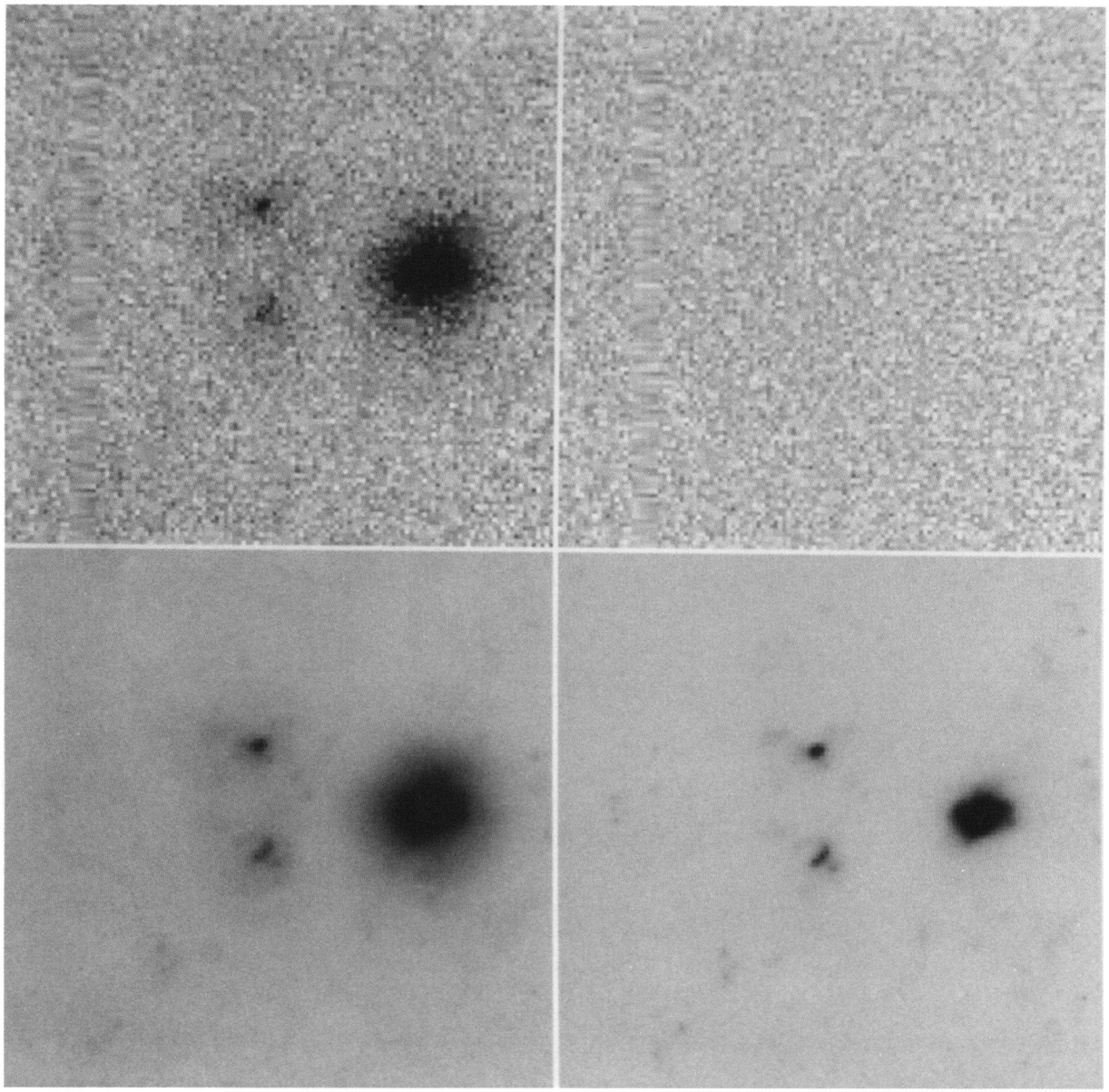

FIG. 15.—Example of noise reduction and deconvolution. The upper left shows an original image (real data); upper right is the estimated noise field; lower left is the noise-reduced (but still degraded) image, which is then restored (*lower right*) by 25 iterations of the Lucy-Richardson algorithm. (For the deconvolved image, a dynamic range 3 times larger than the others is displayed.)

PHILLIPS et al. (see 444, 38)

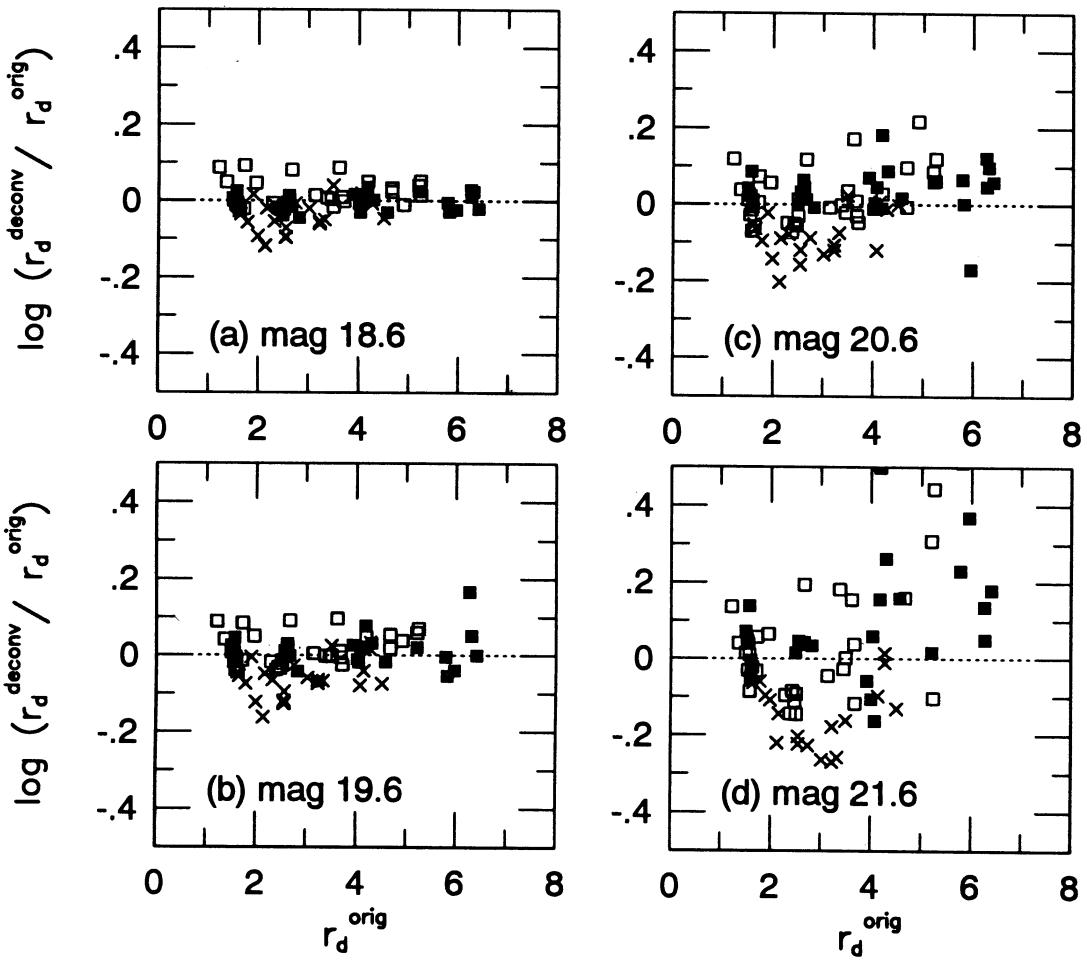

FIG. 16.—Effect of decreasing brightness (i.e., S/N) on the scale lengths measured in deconvolved images. In each case, the deconvolution is 16 accelerated iterations with the Lucy-Richardson algorithm. The four cases differ by 1 mag each; for single-orbit exposures, the approximate magnitudes are (*a*) 18.6, (*b*) 19.6, (*c*) 20.6, and (*d*) 21.6. Early-type galaxies (pure bulge and $D/T = 0.18$) are indicated by (×); intermediate (D/T of 0.43 and 0.62) by open boxes; late (D/T of 0.85 and 1) by filled boxes. Note the strong biases that appear in the faintest case, correlated with galaxy type.

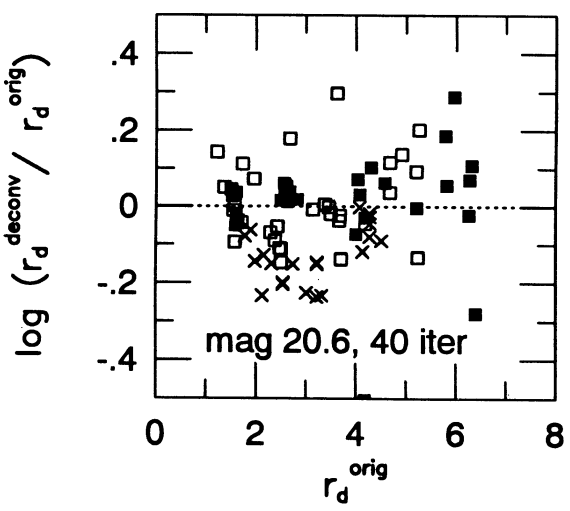

FIG. 17

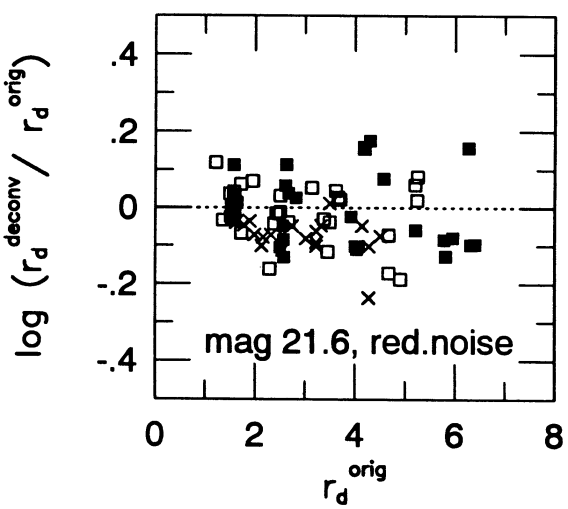

FIG. 18

FIG. 17.—Same as Fig. 16*c*, but with 40 iterations. The scatter has increased significantly with more iterations, and systematic biases have also become much stronger, particularly among the early-type galaxies.

FIG. 18.—Same as Fig. 16*d*, except that an estimated noise field was subtracted prior to deconvolution. The systematic biases are greatly reduced in this case, and the scatter is also significantly reduced.

Since the systematic errors do not become severe—even with the standard Lucy-Richardson algorithm without "noise reduction"—until magnitudes fainter than our completeness limit of $I_{785} \sim 20.4$ (corresponding to case [*c*] in Fig. 16), it is clear that our use of the "noise-reduction" procedure with our actual sample images provides a conservative approach to deconvolution.

Comparing the magnitudes and sizes with Table 3, it is clear that the models overlap well with the observed galaxy parameters. We note that both the models and the galaxies are, on the whole, significantly brighter and larger than the models studied by Schade & Elson (1993). All of their models but one have a disk scale length less than 0".2. While Schade & Elson concluded from their simulations that deconvolution was inappropriate for faint galaxies imaged by the WFC, we find the opposite is true for the galaxies in our sample. Windhorst et al. (1994) arrive at a conclusion similar to ours from different considerations.

REFERENCES

Baxter, D., et al. 1993, STScI preprint 751
Bershady, M. A. 1995, AJ, 109, 87
Bershady, M. A., Hereld, M., Kron, R. G., & Koo, D. C. 1994, AJ, 108, 870
Broadhurst, T. J., Ellis, R. S., & Shanks, T. 1988, MNRAS, 235, 827
Burrows, C., et al. 1991, ApJ, 369, L21
Casertano, S., Ratnatunga, K., Griffiths, R. E., Neuschaefer, L. W., & Windhorst, R. A. 1995, ApJ, submitted
Colless, M. M., Ellis, R. S., Broadhurst, T. J., Taylor, K., & Peterson, B. A. 1993, MNRAS, 261, 19
Colless, M. M., Ellis, R. S., Taylor, K., & Hook, R. N. 1990, MNRAS,
de Vaucouleurs, G., de Vaucouleurs, A., & Corwin, H. G., Jr. 1976, Second Reference Catalog of Bright Galaxies (Austin: Univ. Texas Press) (RC2)
Dressler, A., & Gunn, J. E. 1992, ApJS, 75, 1
Dressler, A., Oemler, A., Gunn, J. E., & Butcher, H. 1993, ApJ, 404, L45
Elson, R. A. W., Forbes, D. A., & Gilmore, G. F. 1994, PASP, 106, 632
Forbes, D. A., Elson, R. A. W., Phillips, A. C., Illingworth, G. D., & Koo, D. C. 1994, ApJ, 437, 17
Forbes, D. A., & Thomson, R. C. 1992, MNRAS, 254, 723
Geisler, D. 1988, NOAO Newsletter, 13, 22
Giraud, E. 1992, A&A, 257, 501
Griffiths, R. E., et al. 1994a, ApJ, 437, 67 (G94)
———. 1994b, ApJ, 435, L19
Gronwall, C. 1994, private communication
Hall, P., & Kackay, C. D. 1984, MNRAS, 210, 979
Harris, H. C., Baum, W. A., Hunter, D. A., & Kreidl, T. J. 1991, AJ, 101, 677
Hook, R. N., & Lucy, L. B. 1992, ST-ECF Newsletter, 17, 10
Huchra, J. P. 1977, ApJS, 35, 171
Infante, L. 1987, A&A, 183, 177
Jarvis, J. F., & Tyson, J. A. 1981, AJ, 86, 476
Kent, S. M. 1984, ApJS, 56, 105
———. 1985, ApJS, 59, 115
Koo, D. C. 1986, ApJ, 311, 651
Koo, D. C. Gronwall, C., & Bruzual, A. G. 1993, ApJ, 415, L21
Koo, D. C., & Kron, R. G. 1992, ARA&A, 30, 613
Kormendy, J., & Djorgovski, S. 1989, ARA&A, 27, 235
Krist, J. 1992, TINYTIM Users Manual, Version 2.1 (Baltimore: STScI)
Kron, R. G. 1980, ApJS, 43, 305
Lauer, T. R. 1989, PASP, 101, 445
Lauer, T. R., et al. 1992, AJ, 104, 552
Lavery, R. J., Pierce, M. J., & McClure, R. D. 1992, AJ, 104, 2067
Lilly, S. J. 1993, ApJ, 411, 501
Lilly, S. J., Cowie, L. L., & Gardner, J. P. 1991, ApJ, 369, 79
Majewski, S. R. 1992, ApJS, 78, 87
Mutz, S. B., et al. 1994, ApJ, 434, L155
Neuschaefer, L. W., & Windhorst, R. A. 1995, ApJ, 439, 14
Neuschaefer, L. W., Castertano, S., Griffiths, R. E., & Ratnatunga, K. 1995, ApJ,, submitted
Phillips, A. C. 1993, Ph.D. thesis, Univ. Washington
Phillips, A. C., Forbes, D. A., Bershady, M. A. Illingworth, G. D., & Koo, D. C. 1994, AJ, 107, 1904
Ratnatunga, K., et al. 1995, in preparation
Ratnatunga, K., Griffiths, R. E., Castertano, S., Neuschaefer, L., & Wyckoff, E. W. 1994, AJ, 108, 2362
Sandage, A., & Bedke, J. 1988, Atlas of Galaxies (NASA SP-496) (Washington, DC: NASA)
Sandage, A., & Tammann, G. A. 1981, A Revised Shapley-Ames Catalog of Bright Galaxies, Carnegie Inst. Washington Publ. 635 (RSA)
Schade, D. J., & Elson, R. A. W. 1993, AJ, 105, 1581
Schechter, P. 1976, ApJ, 203, 297
Tyson, J. A. 1988, AJ, 96, 1
Windhorst, R. A., et al. 1991, ApJ, 380, 362
Windhorst, R., Mathis, D. F., & Keel, W. C. 1992, ApJ, 400, L1
Windhorst, R. A., et al. 1994, AJ, 107, 930